

Supporting Information

Covalent Organic Framework Hydrogel for Synergistic Seawater Desalination and Uranium Extraction

Wei-Rong Cui,^{a†} Cheng-Rong Zhang,^{a†} Ru-Ping Liang,^{a*} and Jian-Ding Qiu^{a,b*}

^aCollege of Chemistry, Nanchang University, Nanchang 330031, China

^bCollege of Materials and Chemical Engineering, Pingxiang University, Pingxiang 337055, China

[†]These authors contributed equally: Wei-Rong Cui, Cheng-Rong Zhang.

*Corresponding authors. Tel/Fax: +86-791-83969518. E-mail: rpliang@ncu.edu.cn; jdqiu@ncu.edu.cn.

Table of Contents

1. Supporting Experimental Section.....	3
2. Supporting Figures and Tables.....	10
3. Supporting References.....	48

1. Supporting Experimental Section

Instruments. Fourier-transform infrared (FT-IR) spectra were recorded on a Nicolet Impact 410 FT-IR spectrometer. Powder X-ray diffraction (PXRD) data of the nanomaterials were collected on a Bruker AXS D8 Advance A25 Powder X-ray diffractometer (40 kV, 40 mA) using Cu K α ($\lambda=1.5406 \text{ \AA}$) radiation. The morphology of the material was imaged by a scanning electron microscope (SEM, JEM-2010, JEOL). X-ray photoelectron spectroscopy (XPS) spectra were performed on a Thermo VG Multilab 2000X with Al K α irradiation. The radiation stabilities of COFs were investigated in a GAMMATOR M-38-2 (USA) irradiator with a ^{60}Co source (γ -ray). The hydrophilic property of the COFs was observed on a contact angle measuring instrument (JY-82B Kruss DSA). EPR spectra were recorded on a Bruker EPR A300 spectrometer. Solid-state ^{13}C cross-polarization magic-angle spinning (^{13}C CP/MAS NMR) spectra were recorded with a 4-mm double-resonance MAS probe; operating at a resonance frequency of 150 MHz, a sample spinning rate of 10.0 kHz, a contact time of 2 ms (ramp 100), and a pulse delay of 3 s were applied. The nitrogen adsorption and desorption isotherms were measured at 77 K using a Micromeritics ASAP 2020M system. The samples were outgassed at 120 °C for 12 h before the measurements. Surface areas were calculated from the adsorption data using Brunauer-Emmett-Teller (BET) methods. The pore-size-distribution curves were obtained via the non-local density functional theory (NLDFIT) method. The thermal properties of the nanomaterials were evaluated using a STA PT1600 Linseis thermogravimetric analysis (TGA) instrument over the temperature range of 30 to 800 °C under nitrogen atmosphere with a heating rate of 10 °C/min. Metal ions concentrations were determined using an iCAP Q inductively coupled plasma mass spectrometry (ICP-MS, Thermo Fisher Scientific, USA). The light-absorbing property of samples is measured by an UV-vis-NIR spectrophotometer (LAMBDA950). The compressive stress-strain curves are obtained from the microcomputer-controlled electronic universal testing machine (SHT4106, MTS System Corporation).

Solar Desalination Test. The broadband illumination is supplied by a solar simulator with a controllable solar density. The solar density is measured by a photoradiometer (Perfectsolar PL-MW2000). A beaker containing the floating evaporator and saline water is placed on an electronic balance (Sartorius, BSA124S-CW, accuracy: 0.1 mg) for real-time measurements of water mass. The probe of an electronic temperature logger (Jingchuang, GSP-6) is inserted into the top layer of the evaporators and an IR camera (FORTRIC 220s) is used to record the temperature vibrations. The seawater collected from the East China Sea near the Xiamen City, Fujian Province was used. The simulated sewage water was prepared using 20 mg L⁻¹ methylene blue or methyl orange. All experiments of solar evaporation and desalination have been completed under the following conditions: the ambient temperatures are 23 ± 2 °C, controlled by an air conditioner and the ambient humidity is 30 ± 5%.

Energy conversion efficiency (η) can be defined as the following equation (1):

$$\eta = (mh_{LV})/q_i \quad (1)$$

Where, m is the solar water evaporation rate of water under solar illumination ($m=m_{\text{light}} - m_{\text{dark}}$, $m_{\text{dark water}}=0.011 \text{ kg m}^{-2} \text{ h}^{-1}$, $m_{\text{dark blank hydrogel}}=0.042 \text{ kg m}^{-2} \text{ h}^{-1}$ in our work), q_i is the power density of solar simulator in the process of solar water evaporation experiment. h_{LV} refers to the sensible heat and the enthalpy of the total liquid-vapor phase-change, which is calculated using the equation (2):

$$h_{LV} = C\Delta T + \Delta h \quad (2)$$

Where, C is the specific heat capacity of water (4.18 j g⁻¹ k⁻¹), ΔT is the increase in water temperature, and Δh is the enthalpy of vaporization on the relative temperature. As reported by previous study, h_{LV} is ca. 2256.4 kJ kg⁻¹.

Stability test. Tp-Sa and Tb-Sa were exposed to the boiling water, γ -ray irradiation (600 kGy), NaOH (9.0 M), and HNO₃ (9.0 M) for 48 h, respectively. The mixture was then filtered and washed with ultra-pure water till the supernatant became neutral and dried under vacuum at 60 °C. Then, the FT-IR spectra and PXRD

patterns were obtained.

Electrochemical studies. Indium-tin oxide (ITO) glasses were firstly cleaned by sonication in ethanol for 30 min and dried under nitrogen flow. 5 mg of COF powder was mixed with 1 mL *n*-BuOH and ultra-sonicated for 30 min to get slurry. 150 μ L of the slurry was spreading onto ITO glass. After air drying, the boundary of the electrode was isolated with epoxy resin. A conventional three electrodes cell was used with a platinum mesh as the counter electrode and an Ag/AgCl electrode (saturated KCl) as reference electrode. The electrolyte was a 5 mM $K_3[Fe(CN)_6]$ aqueous solution and was purged with nitrogen gas for 1 h prior to the measurements. The working electrodes were immersed in the electrolyte for 60 s before any measurements were taken. The photocurrent responses were conducted with a CHI 760E workstation, with the working electrodes irradiated from the front side. The light was generated by a 300W xenon lamp with a light density of 1 kW m⁻² at room temperature with the light wavelength from 300 nm to 2500 nm.

Influence of pH on the uranium adsorption capacity. To determine the optimal pH for uranium uptake, the pH of the solution was adjusted by using HNO₃ or NaOH aqueous solution to 3.0, 4.0, 5.0 and 6.0 respectively. The obtained 5 mg of dry gel was weighed into a transparent glass bottle containing 500 mL (35 ppm) in uranium spiked filtered natural seawater with different pH. The adsorbent was completely suspended by sonication, and then the mixture was moderately stirred at room temperature for 10 h.

Influence of temperature on the uranium adsorption capacity. The obtained 5 mg of dry gel was weighed into a transparent glass bottle containing 500 mL (35 ppm) uranium spiked filtered natural seawater with a pH of 5.0 with moderate magnetic stirring for 10 h. An aliquot was removed and analyzed by using ICP-MS. The uranium adsorption capacities were determined under temperature of 20 °C, 25 °C, and 30 °C, to determine the influence of temperature on the uranium adsorption

capacity.

Uranium adsorption experiments for COF. At ambient conditions, 5 mg Tp-Sa/Tb-Sa was weighed into a transparent glass bottle containing 500 mL (35 ppm) of uranium spiked filtered natural seawater with a pH of 5.0 with moderate magnetic stirring for 10 h. At an interval of 1 h, the treated solution was filtered through a 0.22 μm membrane filter, and the filtrate was collected and analyzed by using ICP-MS to determine the remaining uranium content.

Uranium adsorption experiments. The concentrations of uranium during all the experiments were detected by ICP-MS for extra low concentrations. All the adsorption experiments were performed at ambient conditions. Adsorption experiments were performed according to reported method¹. The uranium adsorption capacity assay was performed by adding 5 mg of dry gel into 500 mL (35 ppm) uranium spiked filtered natural seawater with moderate magnetic stirring at pH 5.0. The uranium spiked filtered natural seawater was irradiated with a xenon lamp having an optical power density of 1 kW m⁻² with the light wavelength from 300 nm to 2500 nm. The treated solution was filtered through a 0.22 μm membrane filter, and the filtrate was collected and analyzed by using ICP-MS to determine the remaining uranium content. The uranium uptake capacity of adsorbent was also determined in natural seawater without additional uranium. In brief, CPP was fixed in the continuous flow of natural seawater to extract uranium (Fig. S61). CPP has a dry mass of 120 mg. The volume of seawater was 1000 L, and the flow rate is controlled at 500 mL/min. The amounts of loaded uranium were determined by ICP-MS at an interval of 1 day. The adsorption capacity at time (q_t , mg/g) was calculated by using equation: $q_t = (C_o - C_t)/m \times V$, where V is the volume of the treated solution (L), m is the amount of used adsorbent (g), C_o is the initial concentration of uranium (mg/L), and C_t is the concentration of uranium (mg/L) at time, respectively.

Recyclability test. After one run of adsorption, the adsorbent was regenerated by

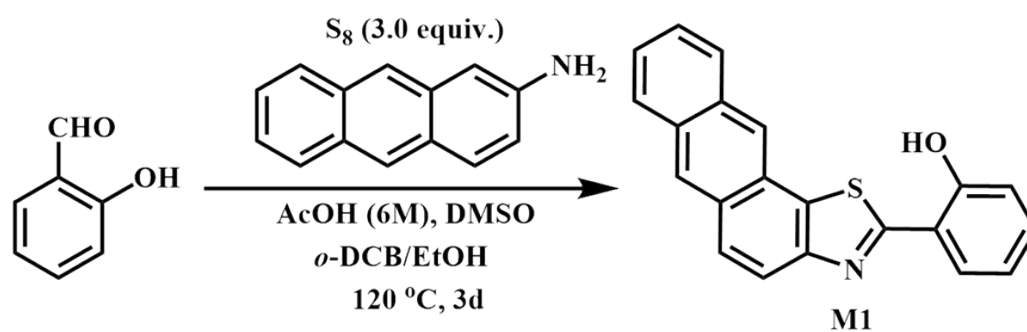
treatment with the elution solution of HNO₃ (0.1 M) and ascorbic acid (0.5 M) and reused for another adsorption experiment. For 5 mg adsorbents, 50 mL elution solution was used to elute the binding uranium and regenerate CPP at room temperature. The elution efficiency (E , %) was determined by using Equation: $E = \frac{C_e \times V_e}{(C_o - C_t) \times V_t} \times 100\%$, in where C_e (mg L⁻¹) is the uranium concentration in elution solution, V_e (L) is the volume elution solution, C_t (mg L⁻¹) is the uranium concentration in uranium-spiked seawater after uranium adsorption, C_o (mg L⁻¹) is the initial uranium concentration of uranium-spiked seawater, V_t (L) is the volume of uranium-spiked seawater used for adsorption.

Influence of bacteria on the uranium adsorption capacity. Antibacterial activity experiments were performed according to reported method¹. The natural seawater was filtered through a 0.22 µm filter to remove insoluble particles and microorganisms. The uranyl nitrate was added into the natural seawater to the final concentration of 35 ppm. The pH of the solution was adjusted to 5.0 after the addition of uranyl nitrate. For each sample, 5.0 mg of dry gel adsorbent and 500 mL uranium spiked natural seawater were used. The simulated sunlight with a light density of 1 kW/m² was used to illuminate the adsorbents. At an interval of 1 h, the treated solution was filtered through a 0.22 µm membrane filter, and the filtrate was collected and analyzed by using ICP-MS to determine the remaining uranium content. The adsorption capacity at time (q_t , mg/g) was calculated by using equation: $q_t = (C_o - C_t)/m \times V$, where V is the volume of the treated solution (L), m is the amount of used adsorbent (g), C_o is the initial concentration of uranium (mg/L), and C_t is the concentration of uranium at time (mg/L), respectively.

Antibacterial activity assay. Antibacterial activity experiments were performed according to reported method¹. The bacterial strains *Vibrio alginolyticus* strain CICC 21664, *Staphylococcus aureus* CICC 10001, *Pseudomonas aeruginosa* strain CICC 10205, and *Bacillus cereus* strain CICC 22802 were used to test the antimicrobial

spectrum of the adsorbents. The exponential growth bacteria and the adsorbents were transferred into fresh LB broth at a ratio of 1% (V/V) and 0.05% (m/V), respectively. After cultivated at 37 °C for 4 h with moderate shaking (180 rpm), the viability of the bacterium was determined. The dilution plate counting method was used according to the Chinese standard GB/T20944 to determine the viability of the adsorbents treated bacterial cultures. In brief, sterilized LB solid medium was poured into the aseptic plates to prepare sterile plate count agar plates under aseptic conditions and bacterial cultures were spread onto the plate after gradient dilution. After cultivating overnight at 37 °C, the number of viable bacterial cells was determined by counting the bacterial clones formed on the plate. The bacterial cultures without treating by adsorbent were used as control. The inhibition rate was calculated using the Equation $IR = (C_i - C_a)/C_i \times 100$, in where C_a (CFU/mL) indicates the concentration of bacterial cultures treated with adsorbent and C_i (CFU/mL) indicates the concentration of bacterial cultures without treatment. The simulated sunlight with a light density of 1 kW m⁻² was used to illuminate the adsorbents.

Synthesis of Model Compound (M1).



2-Hydroxybenzaldehyde (6.1 mg, 0.05 mmol) and anthracen-2-amine (9.6 mg, 0.05 mmol), and sulfur (14.4 mg, 0.45 mmol) were weighed into a 10 mL glass. Acetic acid (6 M, 0.10 mL), DMSO (0.05 mL), *o*-DCB (0.45 mL) and *n*-BuOH (0.50 mL) were then added into the mixture. The mixture was stirred for 10 min, degassed by three freeze-pump-thaw cycles, the sealed tube was placed in an oven at 120 °C for 3 days. The reaction mixture was cooled to room temperature, the precipitate was

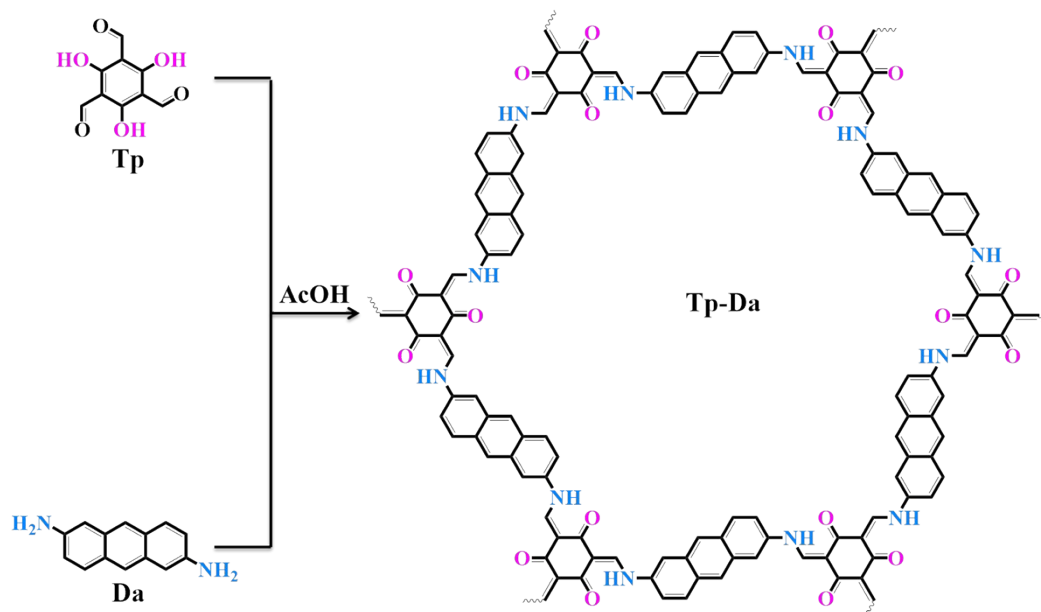
filtered and washed several times with THF. The product was obtained as a pale-yellow solid. Yield: 78%. ^1H NMR (400 MHz, Chloroform-*d*) δ 12.46 (s, 1H), 8.53 (d, $J = 9.0$ Hz, 2H), 8.07 – 8.00 (m, 3H), 7.97 – 7.94 (m, 1H), 7.80 (dt, $J = 7.8, 1.3$ Hz, 1H), 7.58-7.51 (m, 2H), 7.42 – 7.37 (m, 1H), 7.13 (d, $J = 8.3$ Hz, 1H), 7.02 – 6.98 (m, 1H). ^{13}C NMR (101 MHz,) δ 168.08, 157.76, 149.66, 132.49, 132.30, 131.79, 129.54, 128.55, 128.45, 128.13, 128.05, 127.88, 126.61, 126.00, 125.96, 123.20, 120.68, 119.74, 118.05, 117.14,

Synthesis of Tp-Sa. 2,4,6-Triformylphloroglucinol (Tp, 10.50 mg, 0.05 mmol), 2,6-diaminoanthracene (Da, 15.62 mg, 0.075 mmol), and sulfur (14.4 mg, 0.45 mmol) were weighed into a 10 mL glass. Acetic acid (6 M, 0.10 mL), DMSO (0.05 mL), *o*-DCB (0.45 mL) and *n*-BuOH (0.50 mL) were then added into the mixture. The mixture was stirred for 10 min, degassed by three freeze-pump-thaw cycles, the sealed tube was placed in an oven at 120 °C for 3 days. The tube was broken at the neck, and the solid was isolated by centrifugation and washed with acetone (3×5 mL) and THF (3×5 mL). The resulting solid was dried, and then subjected to Soxhlet extraction with toluene and THF as the solvent for two days, respectively, to remove the trapped guest molecules. The powder was collected and dried at 90 °C for 12 h to yield Tp-Sa COF (75%).

Synthesis of Tb-Sa. 1,3,5-Triformylbenzene (Tb, 8.11 mg, 0.05 mmol), 2,6-diaminoanthracene (Da, 15.62 mg, 0.075 mmol), and sulfur (14.4 mg, 0.45 mmol) were weighed into a 10 mL glass. Acetic acid (6 M, 0.10 mL), DMSO (0.05 mL), *o*-DCB (0.45 mL) and *n*-BuOH (0.50 mL) were then added into the mixture. The mixture was stirred for 10 min, degassed by three freeze-pump-thaw cycles, the sealed tube was placed in an oven at 120 °C for 3 days. The tube was broken at the neck, and the solid was isolated by centrifugation and washed with acetone (3×5 mL) and THF (3×5 mL). The resulting solid was dried, and then subjected to Soxhlet extraction with

toluene and THF as the solvent for two days, respectively, to remove the trapped guest molecules. The powder was collected and dried at 90 °C for 12 h to yield Tb-Sa COF (87%).

Synthesis of Tp-Da



The synthesis of Tp-Da COF was performed by the Schiff base condensation reaction between 2,6-diaminoanthracene (Da; 62.4 mg, 0.3 mmol) and 1, 3, 5-triformylphloroglucinol (Tp; 42 mg, 0.2 mmol) in mesitylene (1 mL) – Dioxane (1 mL) solvent mixture with catalytic amount of 8 M Acetic acid (0.2 mL) by typical solvothermal reaction. The reaction mixture was taken in pyrex tube and sonicate for 15 minutes. Following flash frozen at 77K (liquid N₂ bath) and then degassed by three freeze-pump-thaw cycles. After sealing, tube was kept at 120° C for 3 days. A brownish red precipitate was collected by centrifugation and subsequent washing by N, N- dimethylacetamide (N,N- DMA), water and Acetone. Subsequently dried the compound at 150°C by degassing.

Synthesis of PDA. Dopamine hydrochloride (100 mg) are dispersed in Tris-buffer aqueous solution (50 mL, 10 mM; pH 8.5), and then stirred (500 rpm) at ambient

temperature for 12 h. The resulting powders were washed several times using ultrapure water and dried at 60 °C for 12 h.

Synthesis of PVA-PDA hydrogel. In a typical synthesis, PVA (1 g), glutaraldehyde (225 μ L, 50% in ultrapure water), and ultrapure water (10 mL) are mixed together by ultrasonic treatment. Then, HCl (500 μ L, 1.2 M) and PDA (300 mg) solutions were added to the above buffer and the gelation was carried out for 3 h. The obtained PVA-PDA hydrogel was immersed in ultrapure water overnight to obtain pure PVA-PDA hydrogel. The purified PVA-PDA hydrogel was frozen in a refrigerator, and then thawed in ultrapure water at 30 °C. Repeat the freezing and thawing process 3 times. Finally, the obtained PVA-PDA hydrogel was freeze-dried.

2. Supporting Figures and Tables

The core of the structural characterization of Tp-Sa and Tb-Sa was to confirm the formation of the thiazole rings in the frameworks. X-ray photoelectron spectroscopy (XPS) analysis confirmed the presence of nitrogen and sulfur in both Tp-Sa and Tb-Sa (Fig. S1[†]).

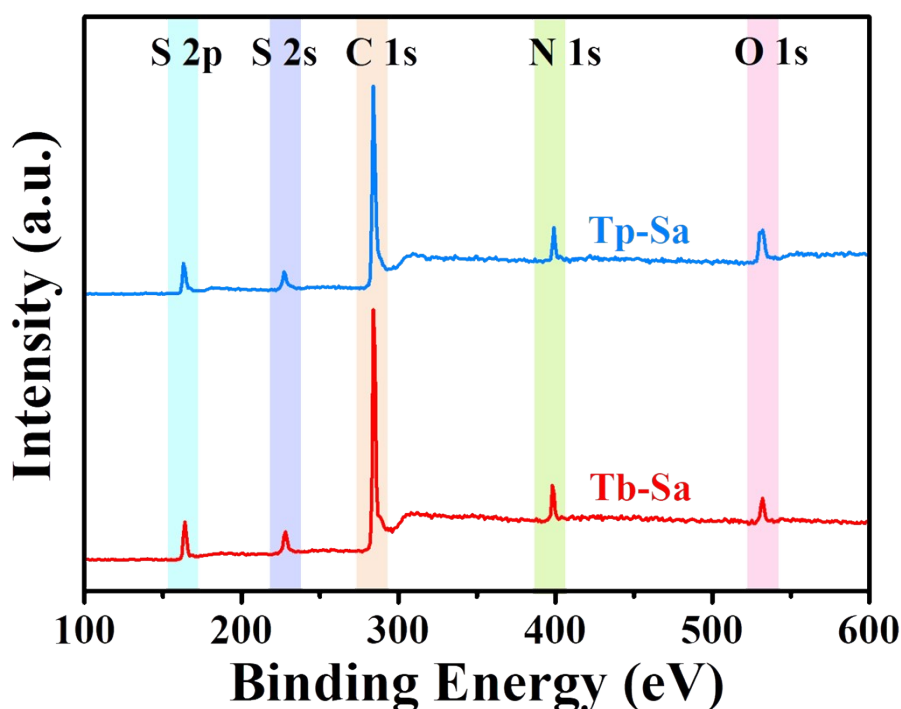


Fig. S1 XPS survey spectra of Tp-Sa and Tb-Sa.

In the FT-IR spectra of Tp-Sa and Tb-Sa (Fig. S2 and S3†), the vibration peaks of the thiazole rings at *ca.* 1597 cm^{-1} (C=N) and *ca.* 795 cm^{-1} (C-S-C) were found, and the vibration peak of C=O (*ca.* 1645 cm^{-1}) completely disappeared,¹ indicating that the thiazole rings was successfully formed and the two COFs were highly condensed.

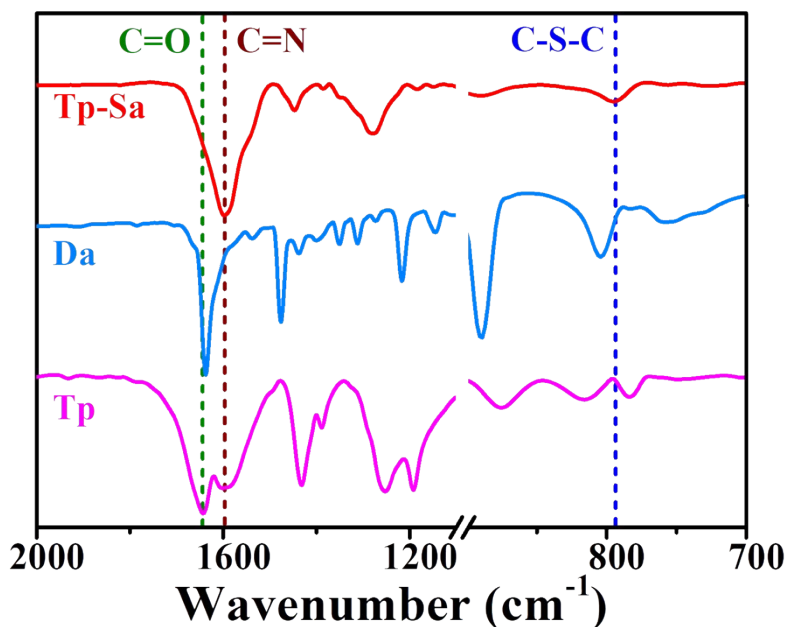


Fig. S2 FT-IR spectra of Tp-Sa, Da and Tp.

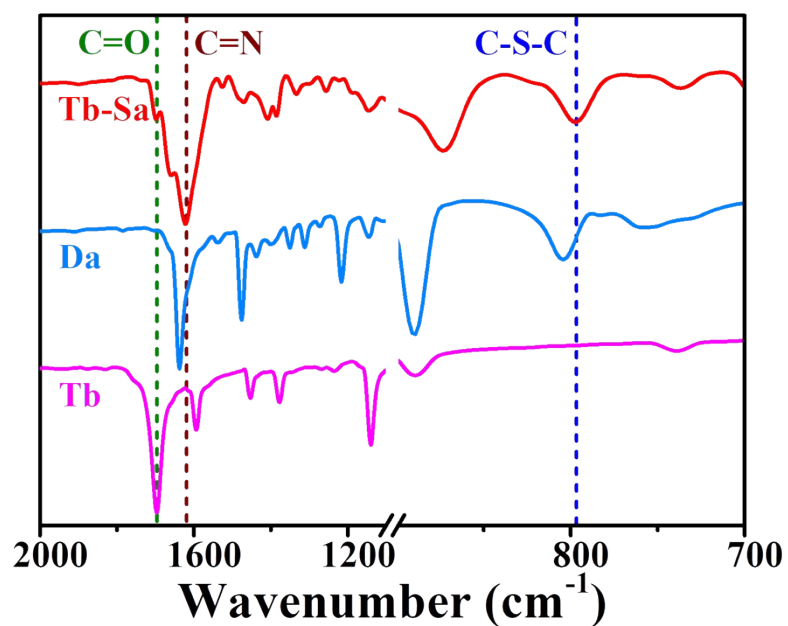


Fig. S3 FT-IR spectra of Tb-Sa, Da and Tb.

The ^{13}C cross-polarization magic-angle spinning (CP/MAS) NMR of Tp-Sa and Tb-Sa further confirmed highly efficient condensation, as demonstrated by the signal located at *ca.* 163 ppm assigned to the carbon atoms in the thiazole rings (Fig. S4 and S5 \dagger).¹ To prove the successful synthesis of thiazole COF, the corresponding thiazole model compound with hydroxyl groups (named M1) and imine linkage COF (named Tp-Da) were synthesized for comparison with Tp-Sa. In the solid-state ^{13}C NMR spectrum of Tp-Da, the signal located at *ca.* 146 ppm was attributed to the C–N, which was consistent with the keto–enol tautomerized structure (Fig. S6 \dagger). While the model compound (M1) and Tp-Sa both showed the same peak at *ca.* 163 ppm, which was assigned to the thiazole carbon S–C=N, providing further evidence of the thiazole units in the framework.

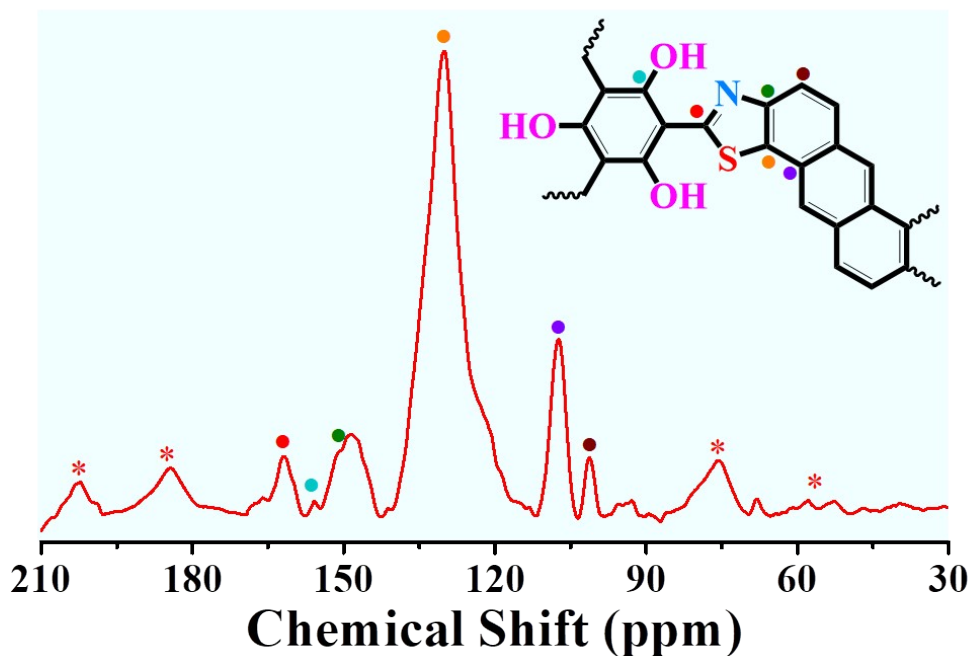


Fig. S4 Solid-state ^{13}C CP/MAS NMR spectrum of Tp-Sa. Spinning side bands are marked with asterisk (*).

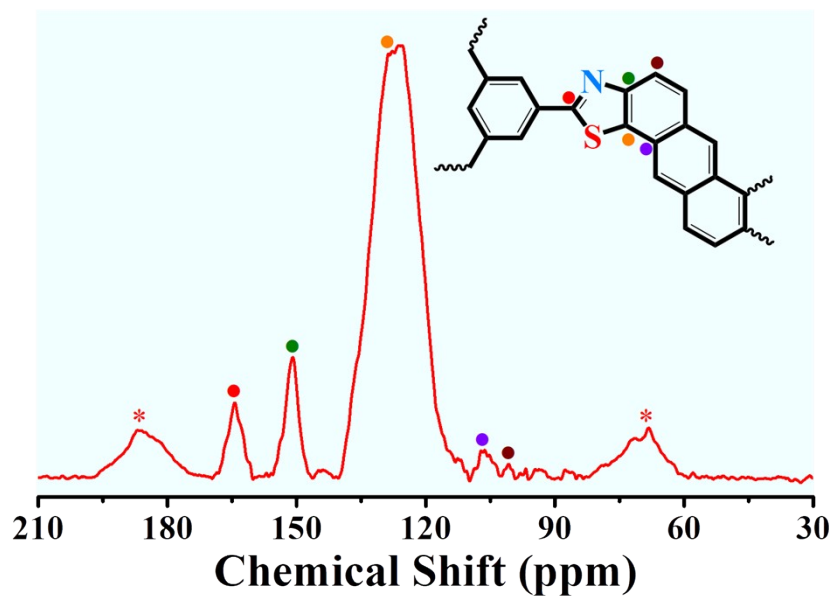


Fig. S5 Solid-state ^{13}C CP/MAS NMR spectrum of Tb-Sa. Spinning side bands are marked with asterisk (*).

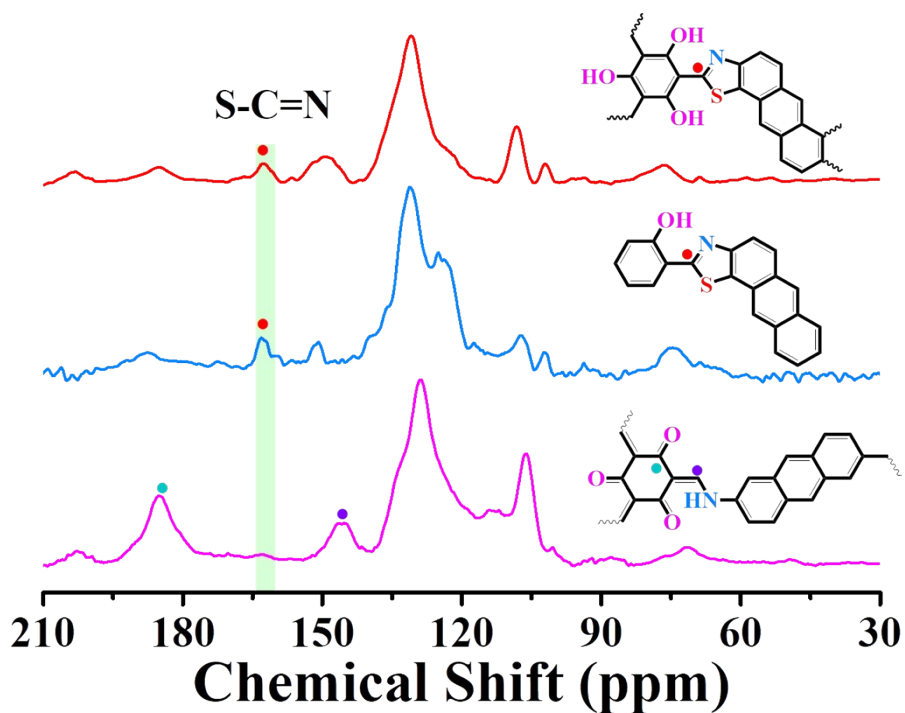


Fig. S6 Solid-state ^{13}C CP/MAS NMR spectrum of Tb-Sa (red line), M1 (blue line) and Tp-Da (pink line).

The crystallinity of Tp-Sa and Tb-Sa was evaluated by powder X-ray diffraction (PXRD) analysis (Fig. S7 and S8†). The PXRD pattern of Tp-Sa exhibited an intense peak at 3.5°, which correspond to the (100) plane, and four other peaks at 6.2°, 7.1°, 9.4° and 25.3°, which correspond to the (110), (200), (220) and (001) planes (Fig. S7b), respectively. Similarly, the PXRD pattern of Tb-Sa showed five distinctive peaks at 3.6°, 6.3°, 7.2°, 9.6° and 25.3° (Fig. S8b). Simulation of their diffraction profiles indicated that Tp-Sa and Tb-Sa matched well with the eclipsed AA-stacking modes (Tables S1 and S2†), and the Pawley refined profiles fitted well with the experimental data ($R_{wp} \leq 2.61\%$ and $R_p \leq 2.12\%$), as evidenced by the negligible deviations.

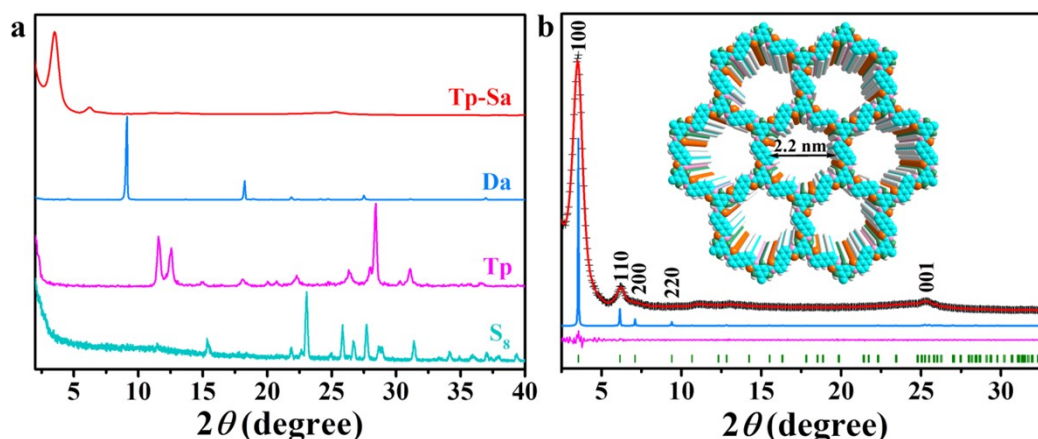


Fig. S7 PXRD patterns of Tp-Sa, Da, and Tp (a). PXRD patterns of Tp-Sa (b): Experimentally PXRD patterns (black cross), Pawley refined profiles (red line), the eclipsed stacking mode (blue line), the refinement differences (pink line), and the Bragg positions (green bar).

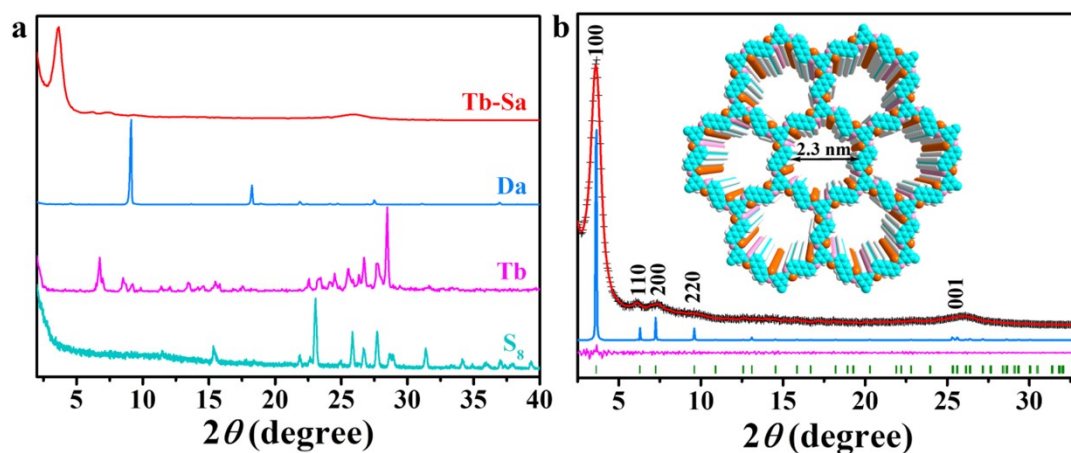


Fig. S8 PXRD patterns of Tb-Sa, Da, and Tb (a). PXRD patterns of Tb-Sa (b): Experimentally PXRD patterns (black cross), Pawley refined profiles (red line), the eclipsed stacking mode (blue line), the refinement differences (pink line), and the Bragg positions (green bar).

Table S1 Fractional atomic coordinates for the eclipsed AA-stacking unit cell of Tp-Sa.

<i>Space group: PM</i>							
$a = 28.7533 \text{ \AA}, b = 3.5281 \text{ \AA}, c = 28.7403 \text{ \AA}$							
$\alpha = \gamma = 90^\circ, \beta = 60^\circ$							
Atom	$x (\text{ \AA})$	$y (\text{ \AA})$	$z (\text{ \AA})$	Atom	$x (\text{ \AA})$	$y (\text{ \AA})$	$z (\text{ \AA})$
C2	0.31496	-1/2	0.28405	C27	0.52804	-1/2	-0.06950
C3	0.37108	-1/2	0.26165	C28	0.47122	-1/2	-0.03716
C4	0.39337	-1/2	0.29602	C29	0.44732	-1/2	0.01892
C5	0.36029	-1/2	0.35382	C30	0.43931	-1/2	-0.06179
C6	0.30272	-1/2	0.37482	C31	0.46371	-1/2	-0.11805
C7	0.40819	-1/2	0.20032	C32	0.51953	-1/2	-0.14875
C8	0.38401	-1/2	0.39185	C33	0.55069	-1/2	-0.12542
C9	0.21813	-1/2	0.36633	S34	0.62009	-1/2	-0.17531
N10	0.46013	-1/2	0.17866	C35	0.60056	-1/2	-0.22755
C11	0.48859	-1/2	0.12200	N36	0.54873	-1/2	-0.20551
C12	0.45686	-1/2	0.09903	C37	0.63709	-1/2	-0.28950
S13	0.38716	-1/2	0.14913	C38	0.61394	-1/2	-0.32412
N14	0.35352	-1/2	0.44372	C39	0.64598	-1/2	-0.38066
C15	0.38060	-1/2	0.47354	C40	0.70269	-1/2	-0.40498
C16	0.43503	-1/2	0.44280	C41	0.72871	-1/2	-0.37364
S17	0.45530	-1/2	0.37334	C42	0.69520	-1/2	-0.31623
S18	0.16744	-1/2	0.43881	C43	0.79053	-1/2	-0.39790
C19	0.11656	-1/2	0.42018	C44	0.62009	-1/2	-0.41631
C20	0.13906	-1/2	0.36557	N45	0.81196	-1/2	-0.36726
N21	0.19566	-1/2	0.33696	C46	0.86872	-1/2	-0.39450
C22	0.47938	-1/2	0.04305	C47	0.89224	-1/2	-0.44904

C23	0.53623	-1/2	0.01059	S48	0.84296	-1/2	-0.46941
C24	0.56839	-1/2	0.03491	N49	0.64943	-1/2	-0.46829
C25	0.54433	-1/2	0.09104	C50	0.62060	-1/2	-0.49599
C51	0.56598	-1/2	-0.46367	O77	0.73004	-1/2	-0.46099
S52	0.54753	-1/2	-0.39404	O78	0.55896	-1/2	-0.30614
C53	0.94811	-1/2	-0.48209	H79	0.61178	-1/2	0.01055
C54	0.98044	-1/2	-0.45758	H80	0.56827	-1/2	0.11052
C55	0.95569	-1/2	-0.40101	H81	0.60342	-1/2	-0.07024
C56	0.89937	-1/2	-0.36925	H82	0.40397	-1/2	0.04370
C57	0.53210	-1/2	-0.48583	H83	0.39590	-1/2	-0.03762
C58	0.55623	-1/2	-0.54272	H84	0.43996	-1/2	-0.13769
C59	0.61256	-1/2	-0.57527	H85	0.97980	-1/2	-0.38168
C60	0.64494	-1/2	-0.55167	H86	0.87961	-1/2	-0.32584
C61	0.46805	-1/2	0.46566	H87	0.63128	-1/2	-0.61867
C62	0.44358	-1/2	0.52247	H88	0.68830	-1/2	-0.57590
C63	0.38701	-1/2	0.55416	H89	0.36765	-1/2	0.59760
C64	0.35529	-1/2	0.52947	H90	0.31194	-1/2	0.55306
C65	0.10786	-1/2	0.34105	H91	0.12696	-1/2	0.29770
C66	0.05186	-1/2	0.37332	H92	0.02730	-1/2	0.35446
C67	0.02793	-1/2	0.42971	H93	0.06143	-1/2	0.52870
C68	0.06059	-1/2	0.45395	H94	0.45744	-1/2	-0.41026
C69	0.03657	-1/2	0.51018	H95	0.94720	-1/2	-0.55665
C70	0.47588	-1/2	-0.45362	H96	0.54250	-1/2	0.39023
C71	0.97205	-1/2	-0.53812	H97	0.27230	-1/2	0.45976
C72	0.52403	-1/2	0.43360	H98	0.47216	-1/2	0.28497
O73	0.26486	-1/2	0.42946	H99	0.25968	-1/2	0.25453
O74	0.44932	-1/2	0.26834	H100	0.70712	-1/2	-0.24930
O75	0.29769	-1/2	0.24647	H101	0.76956	-1/2	-0.48403
O76	0.72362	-1/2	-0.28871	H102	0.52904	-1/2	-0.26818

Table S2 Fractional atomic coordinates for the eclipsed AA-stacking unit cell of Tb-Sa.

<i>Space group: P 6/M</i>							
<i>a = 28.1387 Å, b = 3.5141 Å, c = 3.5145 Å</i>							
<i>α = γ = 90°, β = 60°</i>							
Atom	x (Å)	y (Å)	z (Å)	Atom	x (Å)	y (Å)	z (Å)
C1	0.27600	0.63081	1/2	C9	0.53426	0.55746	1/2
C2	0.31210	0.60992	1/2	C10	0.56816	0.61503	1/2
C3	0.40700	0.62275	1/2	C11	0.54480	0.64891	1/2
N4	0.45983	0.65479	1/2	C12	0.55747	0.52353	1/2
C5	0.48790	0.62482	1/2	H13	0.29546	0.56589	1/2
C6	0.45429	0.56876	1/2	H14	0.61243	0.63360	1/2
S7	0.38288	0.54927	1/2	H15	0.57029	0.69313	1/2
C8	0.47630	0.53371	1/2	H16	0.60170	0.54164	1/2

According to the N₂ adsorption-desorption isotherms, the Brunauer-Emmett-Teller (BET) surface areas of the Tp-Sa and Tb-Sa were calculated to be 880 and 681 m² g⁻¹ (Fig. S9 and S10†), respectively. Based on the nonlocal density function theory (NLDFT) model, the Tp-Sa and Tb-Sa had prominent peaks at 2.06 and 2.14 nm (Fig. S11 and S12†), respectively, which matched well with the AA-stacking models.

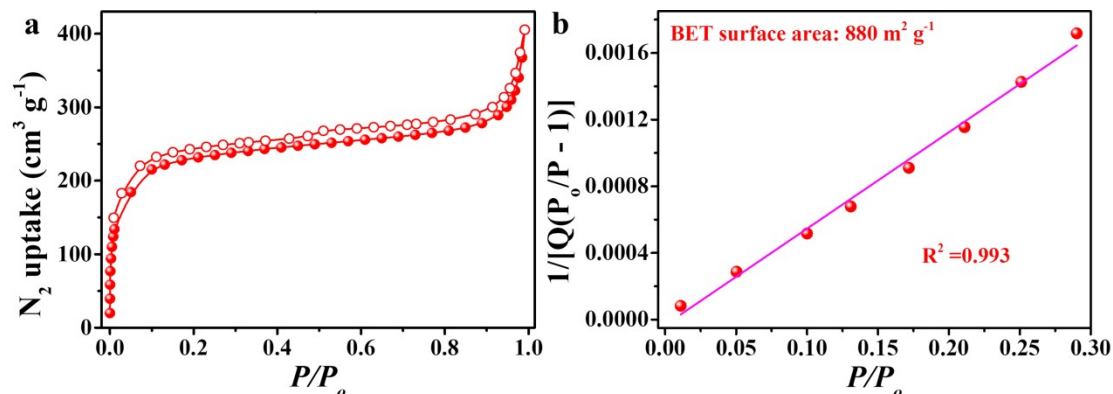


Fig. S9 N₂ adsorption–desorption isotherms of Tp-Sa (a). BET surface area plots of Tp-Sa calculated from the isotherms (b).

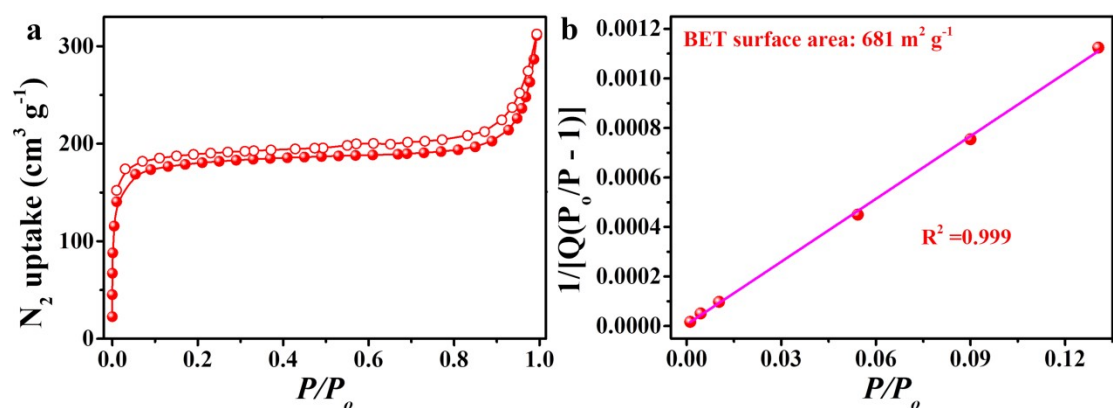


Fig. S10 N₂ adsorption–desorption isotherms of Tp-Sa (a). BET surface area plots of Tb-Sa calculated from the isotherms (b).

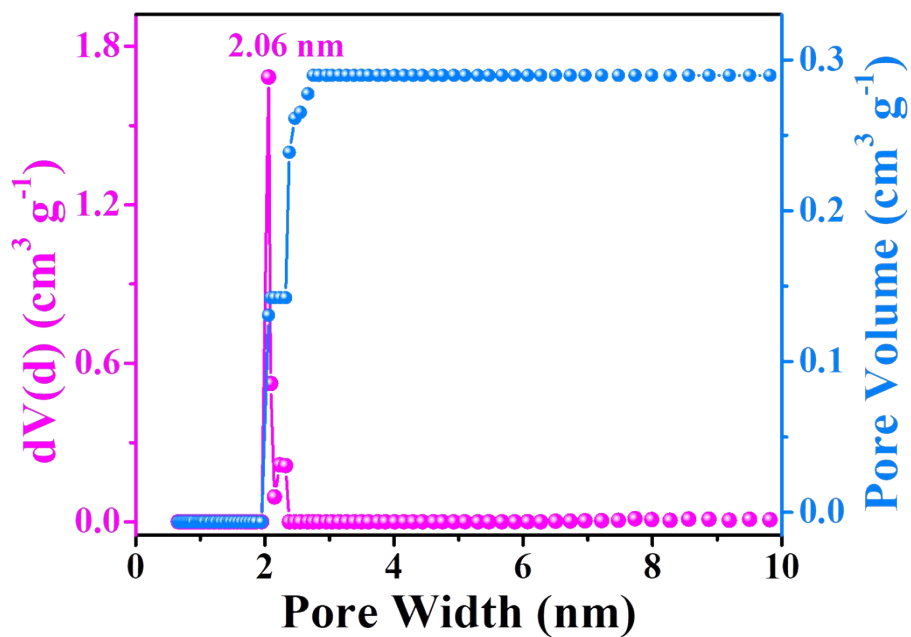


Fig. S11 Pore-size and pore-volume distribution profiles of the Tp-Sa.

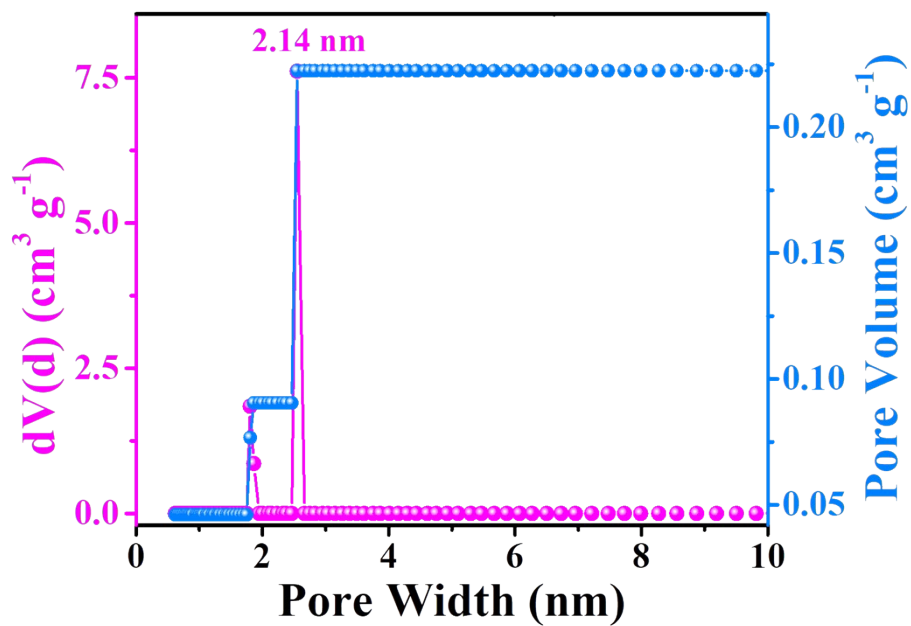


Fig. S12 Pore-size and pore-volume distribution profiles of the Tb-Sa.

In addition, scanning electron microscopy (SEM) images of thiazole-linked COFs showed a cross-linked fiber network structure (Fig. S13 and S14†).

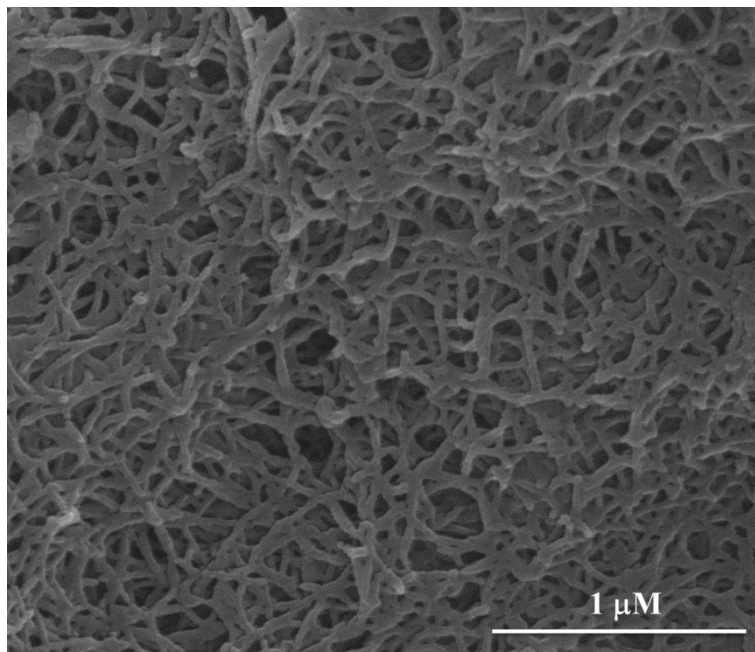


Fig. S13 SEM image of Tp-Sa.

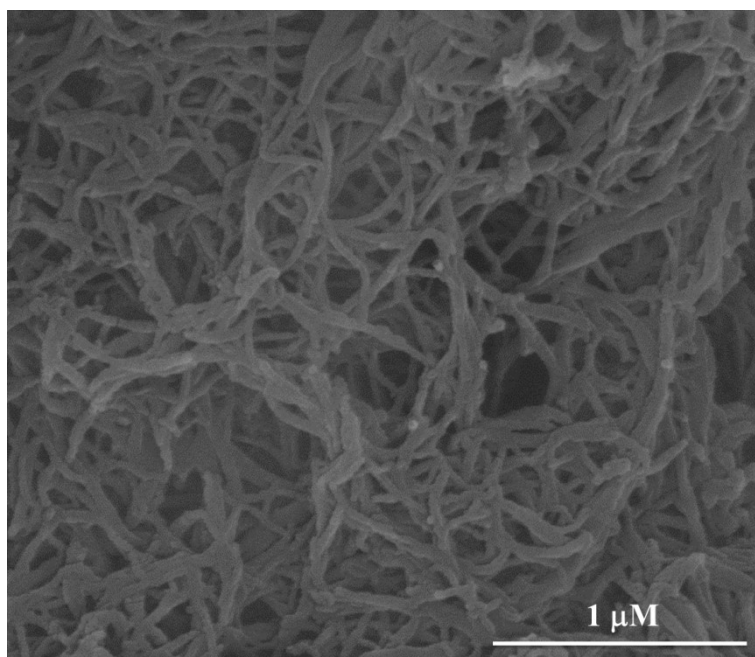


Fig. S14 SEM image of Tb-Sa.

Excellent stability is essential for adsorbents to extract uranium from natural seawater. Owing to the formation of robust thiazole linkages throughout the π -conjugated framework, Tp-Sa and Tb-Sa exhibited exceptional stability. We treated Tp-Sa and Tb-Sa under various severe conditions for 48 h to investigate chemical stability. The PXRD and FT-IR spectra showed that Tp-Sa and Tb-Sa both retained high crystallinity and the same peaks after the treatments (Fig. S15-S18[†]). To fully reflect the superior stability of the thiazole linkages, the imine-based COFs (Tp-Da) was used to performed stability test. After exposure to 12 M HCl and 1 M NaBH₄ solutions for 48 h, the crystallinity of Tp-Da was completely destroyed (Fig. S19[†]), while our Tp-Sa can maintain good crystallinity and stability after treatment with 12 M HCl and 1 M NaBH₄. The results show that thiazole linkages COF has superior stability in high chemical stability compared with imine linkage COF.

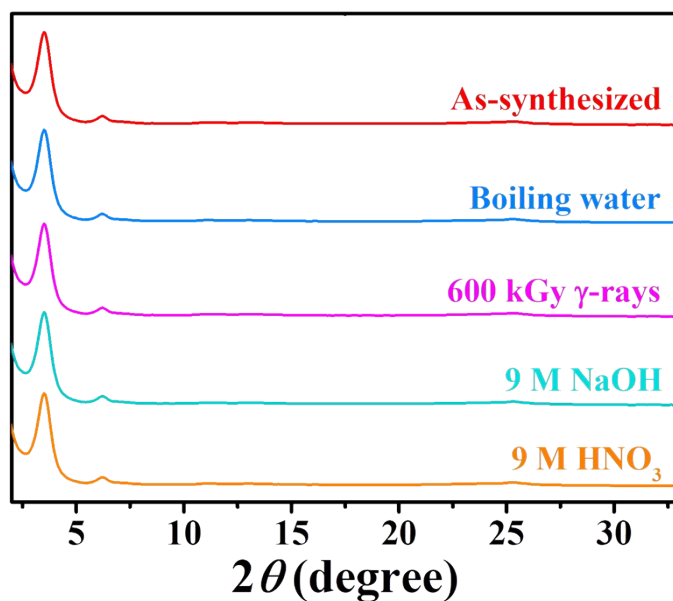


Fig. S15 PXRD patterns of Tp-Sa before and after treatment with boiling water, 600 kGy γ -ray irradiation, 9 M NaOH and 9 M HNO₃.

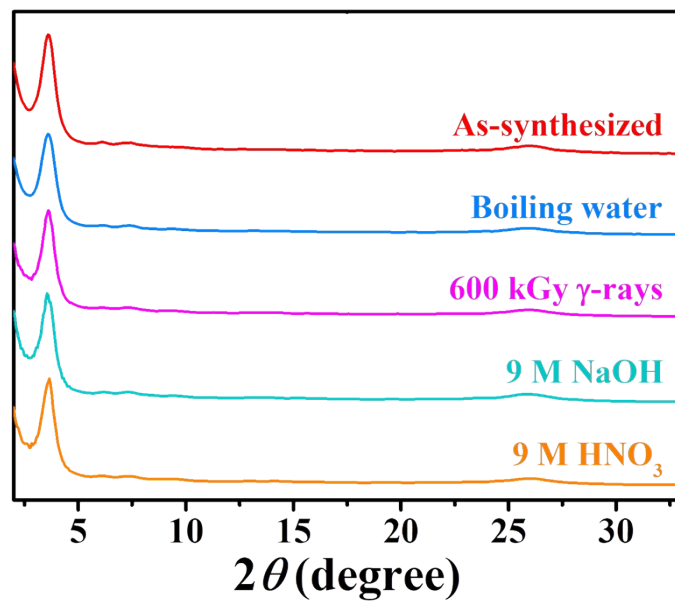


Fig. S16 PXRD patterns of Tb-Sa before and after treatment with boiling water, 600 kGy γ -ray irradiation, 9 M NaOH and 9 M HNO₃.

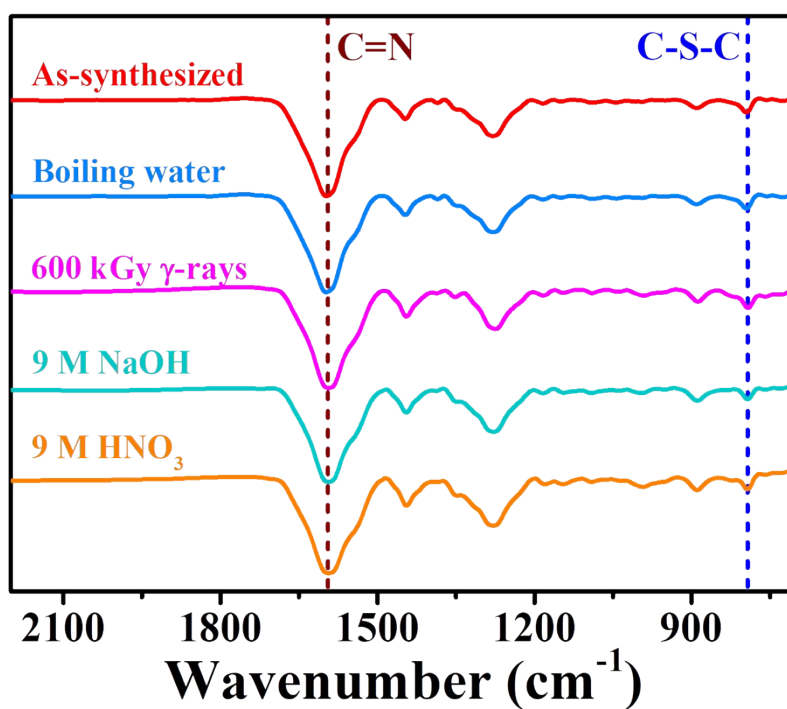


Fig. S17 FT-IR spectra of Tp-Sa before and after treatment with boiling water, 600 kGy γ -ray irradiation, 9 M NaOH, and 9 M HNO₃.

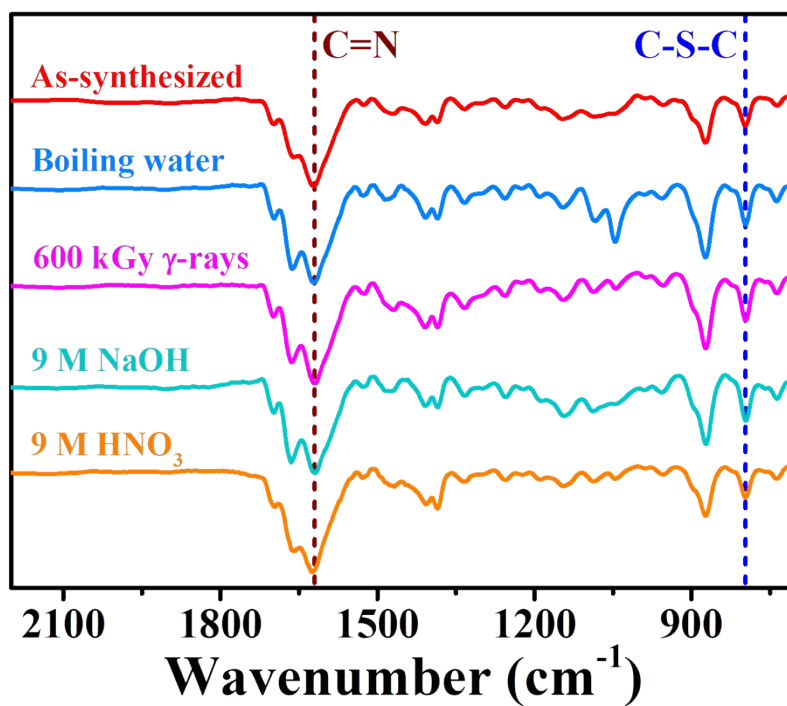


Fig. S18 FT-IR spectra of Tb-Sa before and after treatment with boiling water, 600 kGy γ -ray irradiation, 9 M NaOH, and 9 M HNO₃.

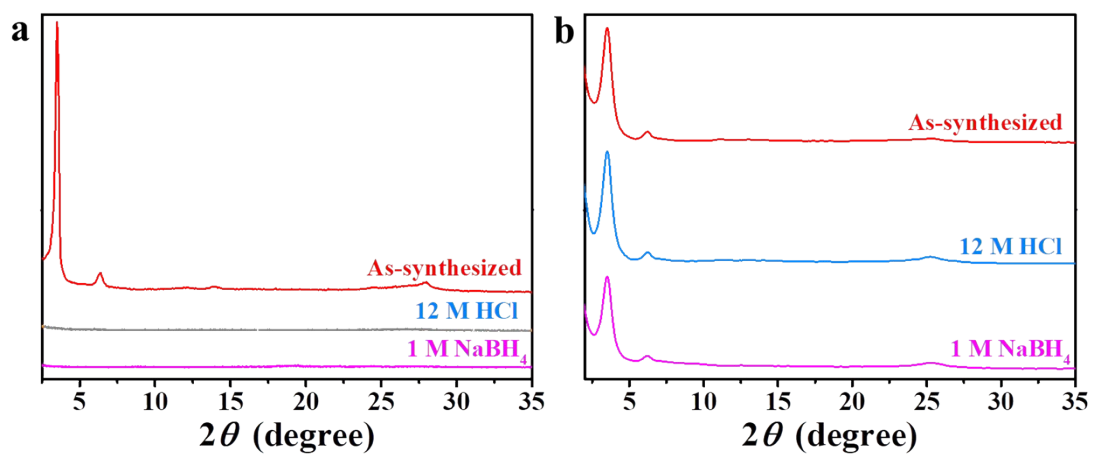


Fig. S19 PXR profiles of (a) Tp-Da and (b) Tp-Sa measured after treatment with 12 M HCl and 1 M NaBH₄ for 48 h.

Thermogravimetric analysis (TGA) curves showed that both Tp-Sa and Tb-Sa were stable up to 450 °C (Fig. S20†). Such high stability is essential for the regeneration of the adsorbent.

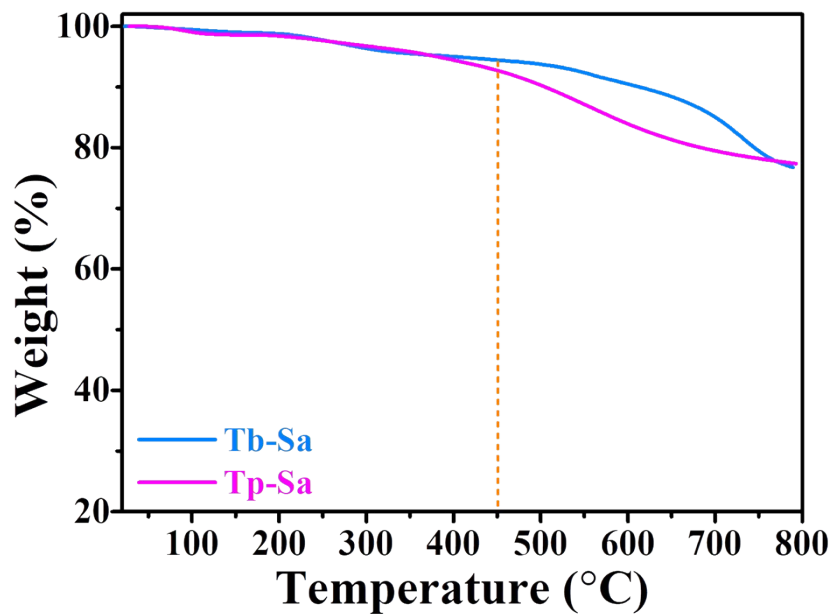


Fig. S20 TGA curves of Tp-Sa and Tb-Sa.

To investigate the hydrophilicity of Tp-Sa and Tb-Sa, their static water contact angles were determined. Due to the introduced dense hydroxyl groups, the hydrophilicity of Tp-Sa was significantly improved compared with Tb-Sa (Fig. S21†).

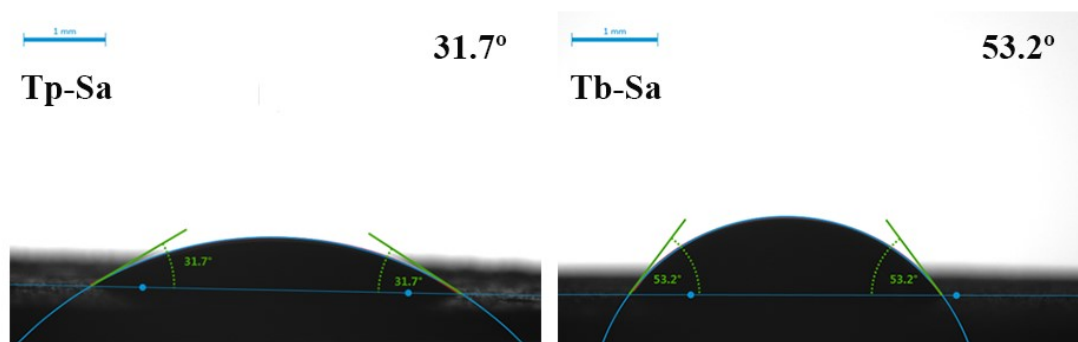


Fig. S21 Static water contact angles of Tp-Sa and Tb-Sa.

In addition, their UV/vis absorption spectra revealed that, compared with the Tb-Sa, Tp-Sa exhibited much higher absorbance over the entire spectrum (250-2500 nm) (Fig. S22†).

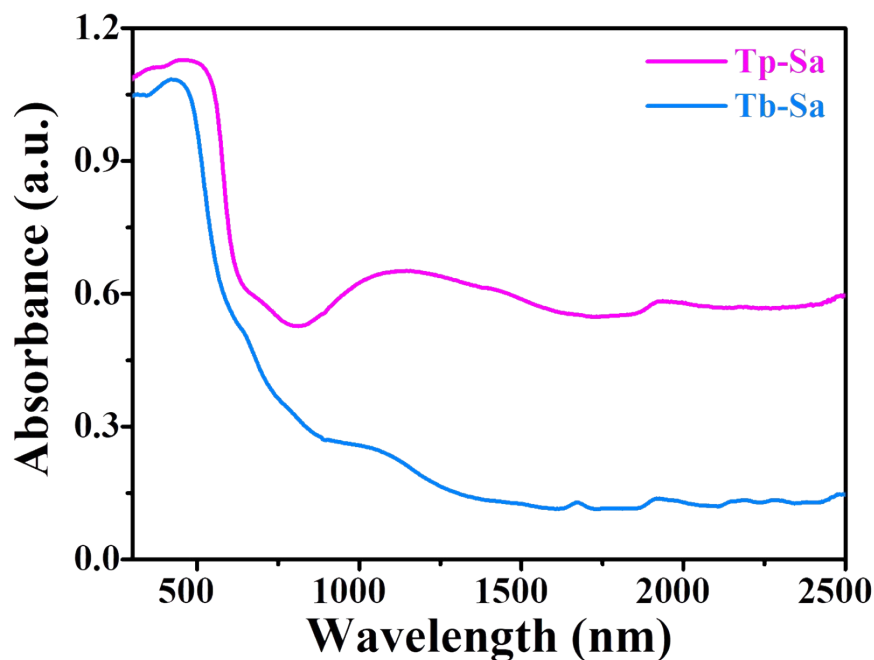


Fig. S22 Absorption spectra of Tp-Sa and Tb-Sa.

The full-spectrum absorption features lay the foundation for the excellent photocatalytic activity of Tp-Sa and Tb-Sa, which was confirmed by electron paramagnetic resonance (EPR) analysis. Compared with Tb-Sa, Tp-Sa showed stronger reactive oxygen species (ROS) signals under visible light irradiation (Fig. S23†). All of these confirmed that the introduction of hydroxyl groups into the robust thiazole-linked COF could greatly increase the capability for visible-light absorption, improve the photocatalytic activity and hydrophilicity, and provide new insights into the design of new functional COFs.

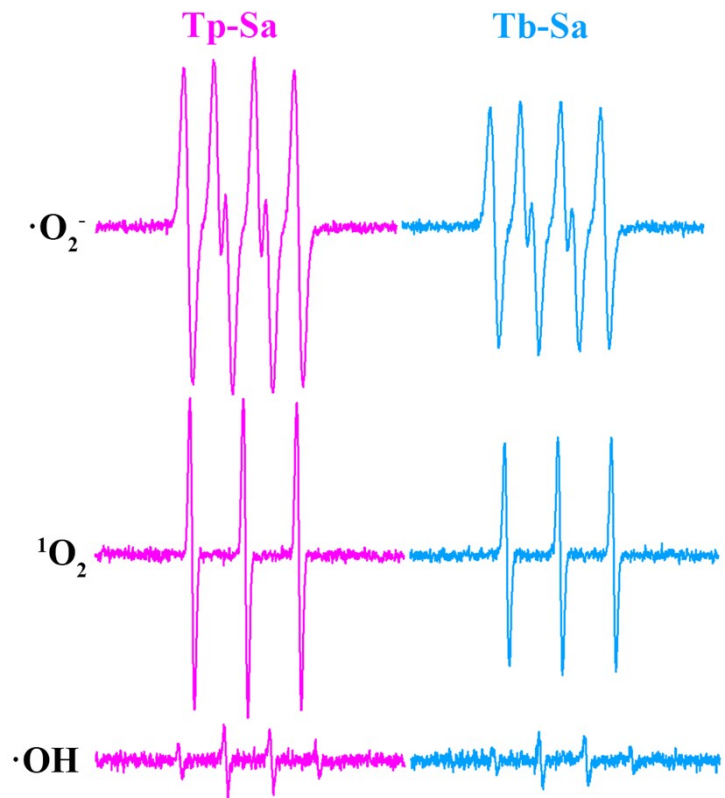


Fig. S23 Production of ROS under visible light irradiation.

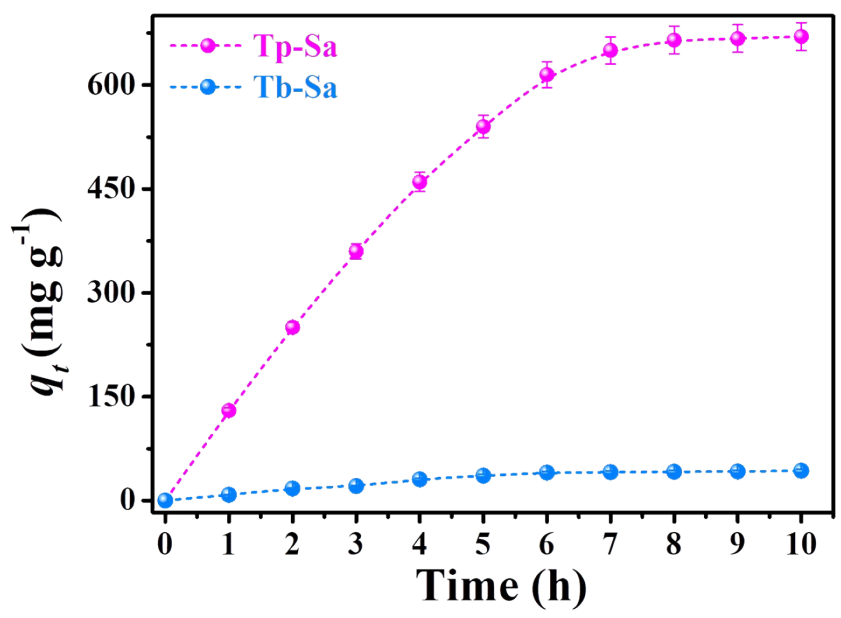


Fig. S24 Uranium extraction capacity of Tp-Sa and Tb-Sa under dark conditions in uranium spiked filtered natural seawater.

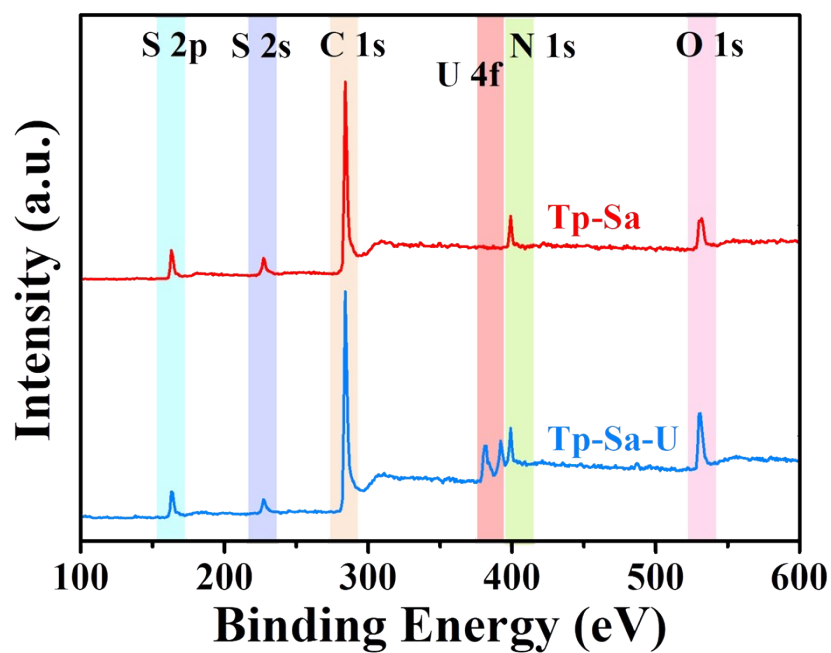


Fig. S25 XPS spectra of Tp-Sa measured before and after uranium extraction.

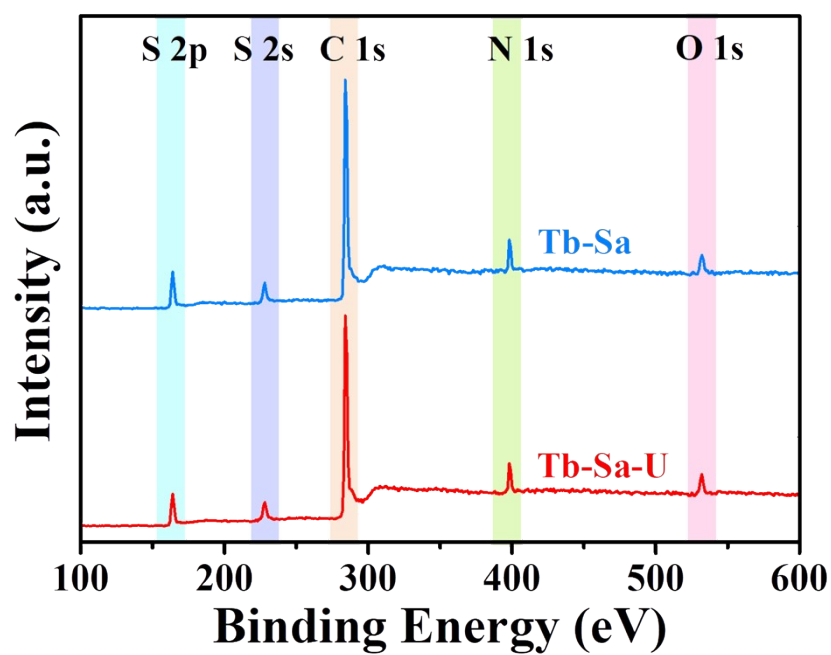


Fig. S26 XPS spectra of Tb-Sa measured before and after uranium extraction.

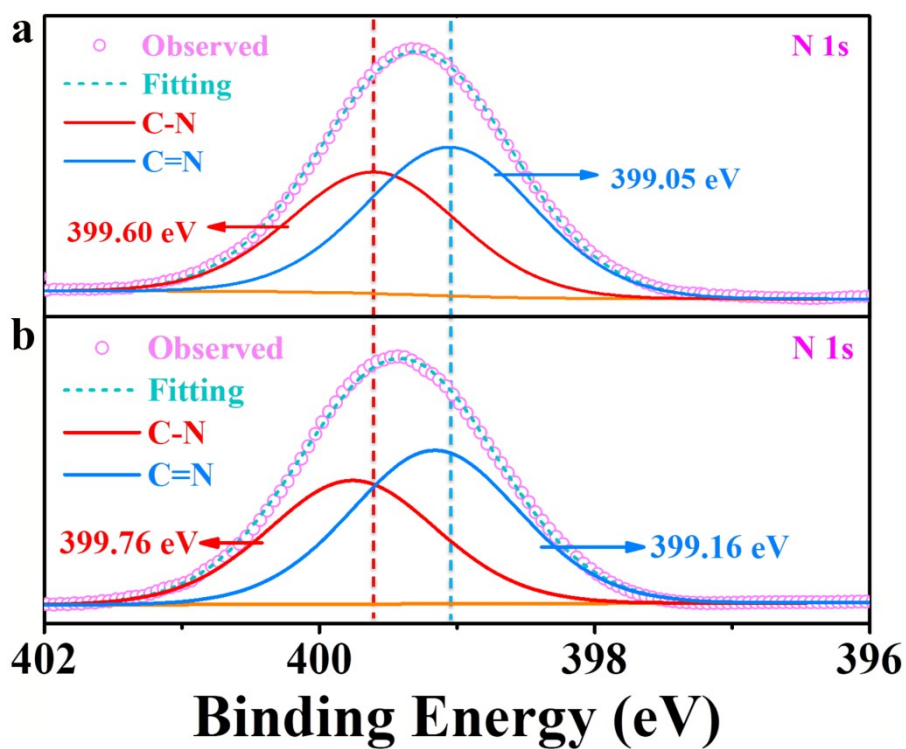


Fig. S27 High-resolution XPS spectra of N 1s for Tp-Sa (a) and Tp-Sa-U (b).

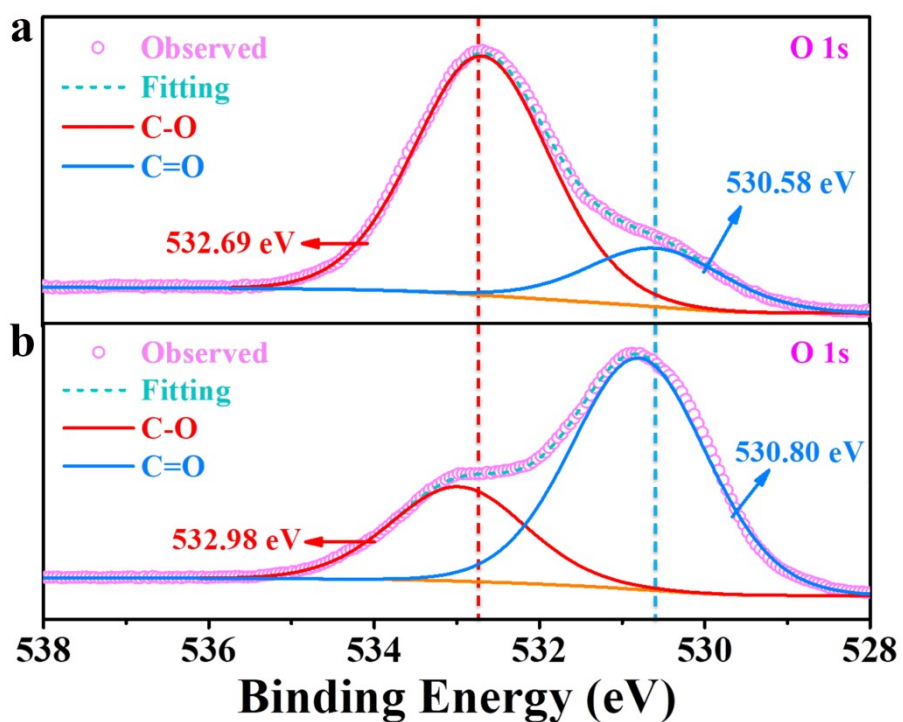


Fig. S28 High-resolution XPS spectra of O 1s for Tp-Sa (a) and Tp-Sa-U (b).

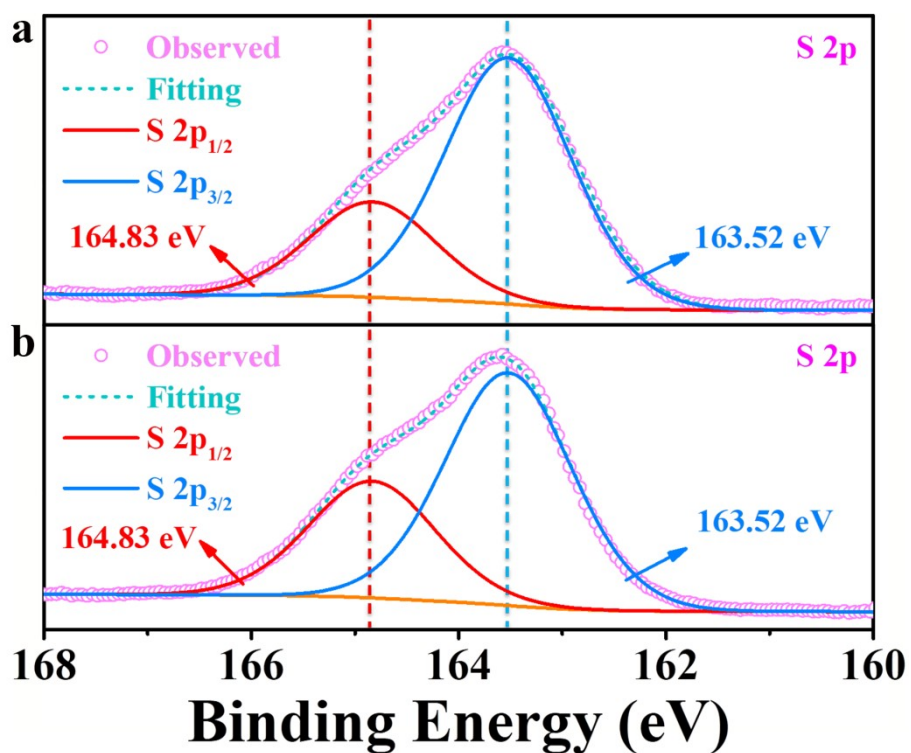


Fig. S29 High-resolution XPS spectra of S 2p for Tp-Sa (a) and Tp-Sa-U (b).

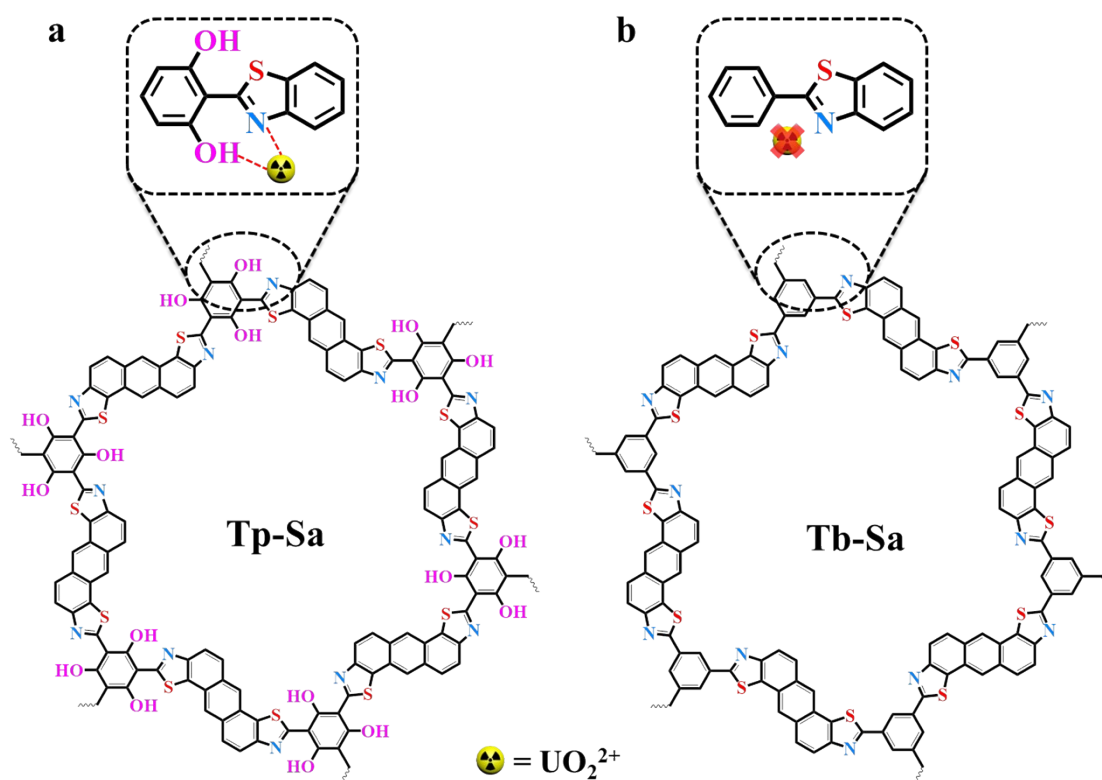


Fig. S30 Schematic diagram of the interaction between Tp-Sa (a) and Tb-Sa (b) and uranyl.

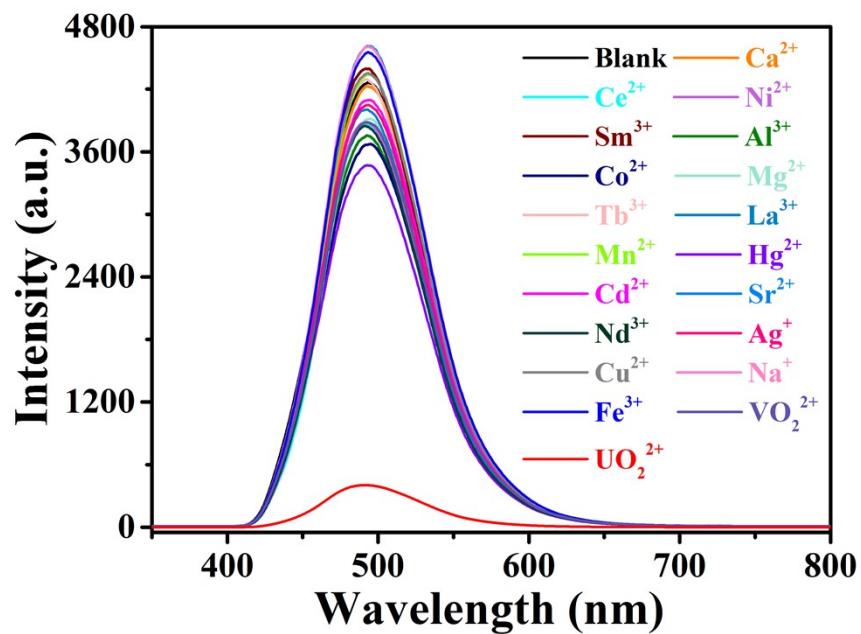


Fig. S31 The emission spectra of Tp-Sa in the presence of various cations. Concentrations of metal ions were 20 μ M.

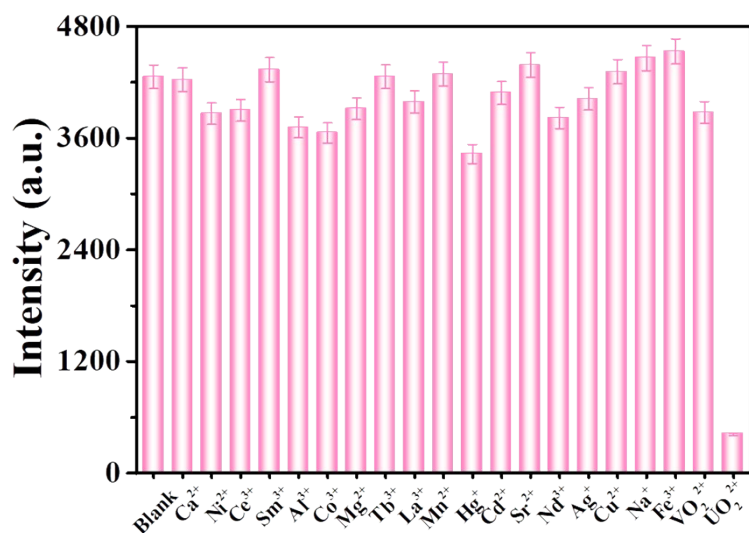


Fig. S32 Fluorescence intensity of Tp-Sa in the presence of various metal ions. Concentrations of metal ions were 20 μ M.

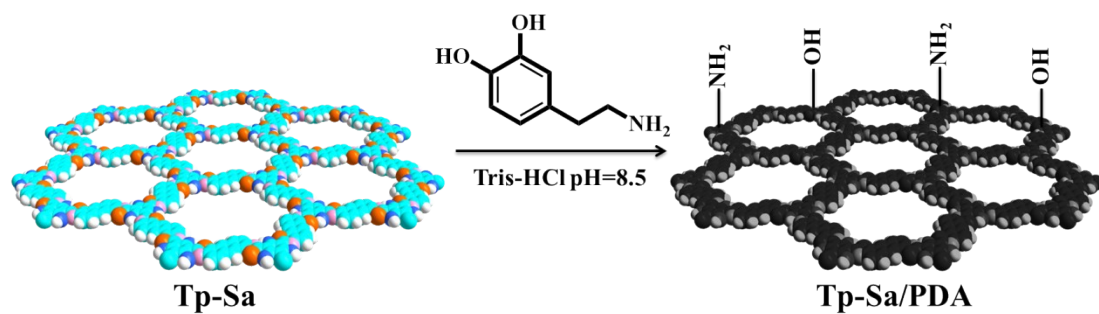


Fig. S33 The synthesis of Tp-Sa/PDA.

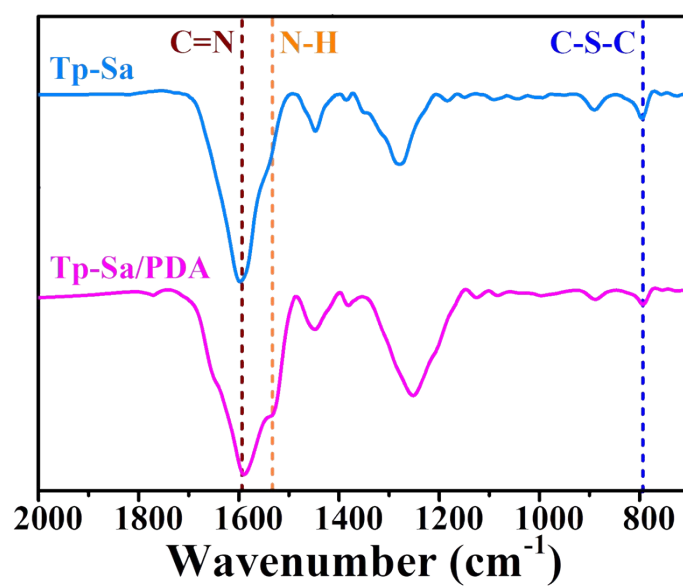


Fig. S34 FT-IR spectra of Tp-Sa and Tp-Sa/PDA.

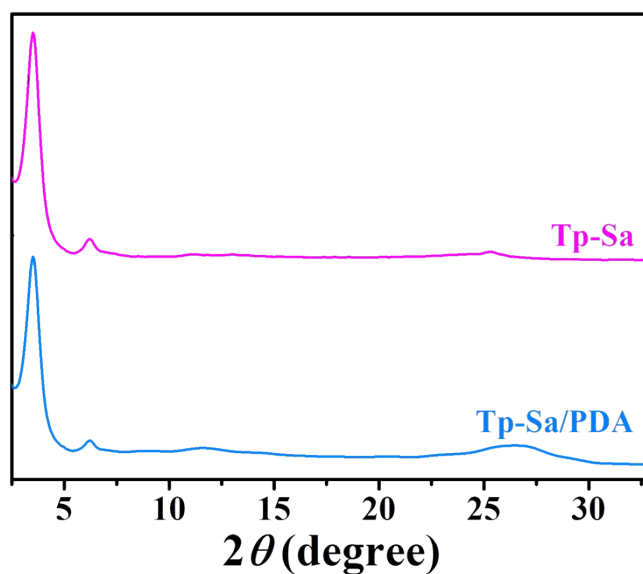


Fig. S35 PXRD profiles of Tp-Sa and Tp-Sa/PDA.

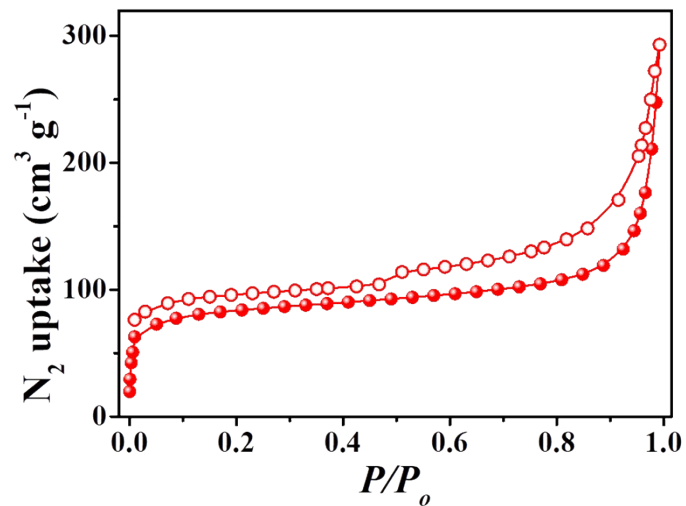


Fig. S36 N₂ adsorption–desorption isotherms of Tp-Sa/PDA.

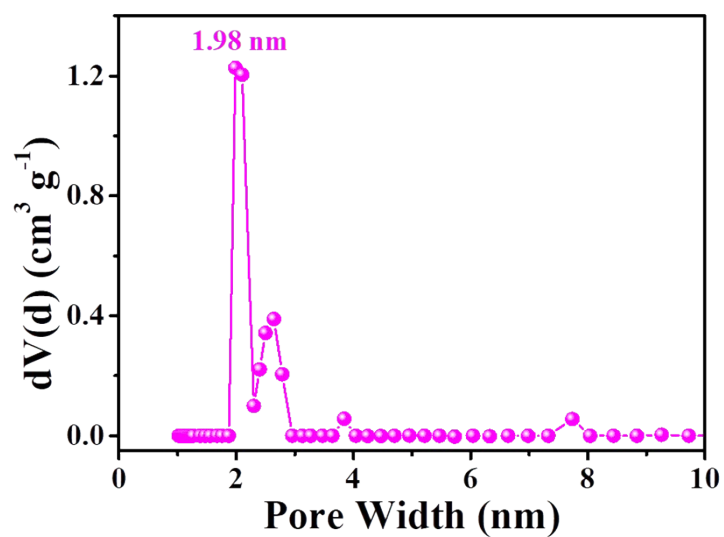


Fig. S37 Pore-size distribution profiles of the Tp-Sa/PDA.

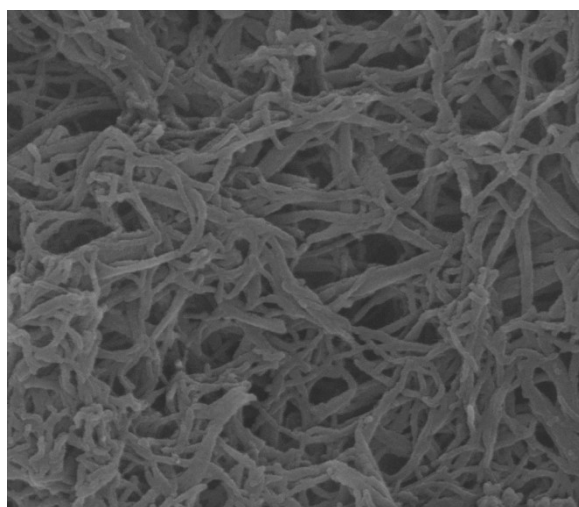


Fig. S38 SEM image of Tp-Sa/PDA.

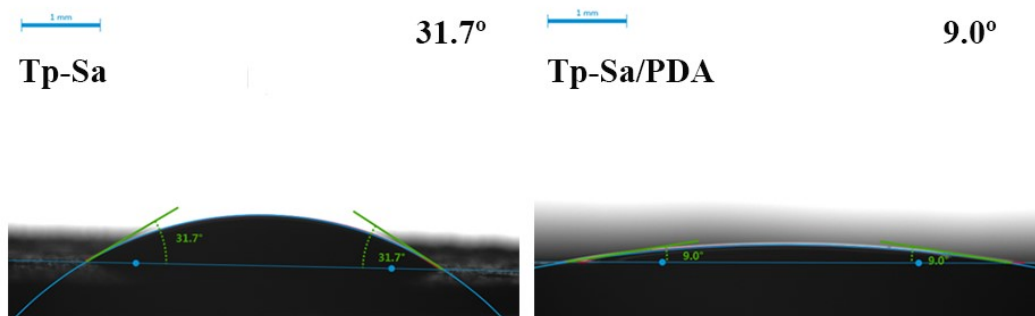


Fig. S39 Static water contact angles of Tp-Sa and Tp-Sa/PDA.

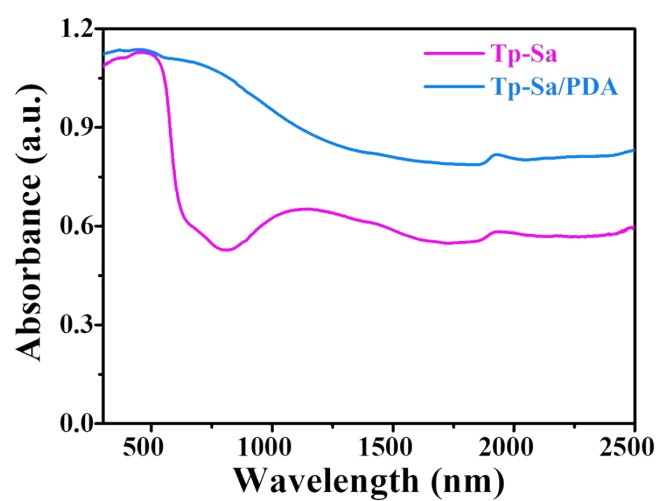


Fig. S40 Absorption spectra of Tp-Sa and Tp-Sa/PDA.

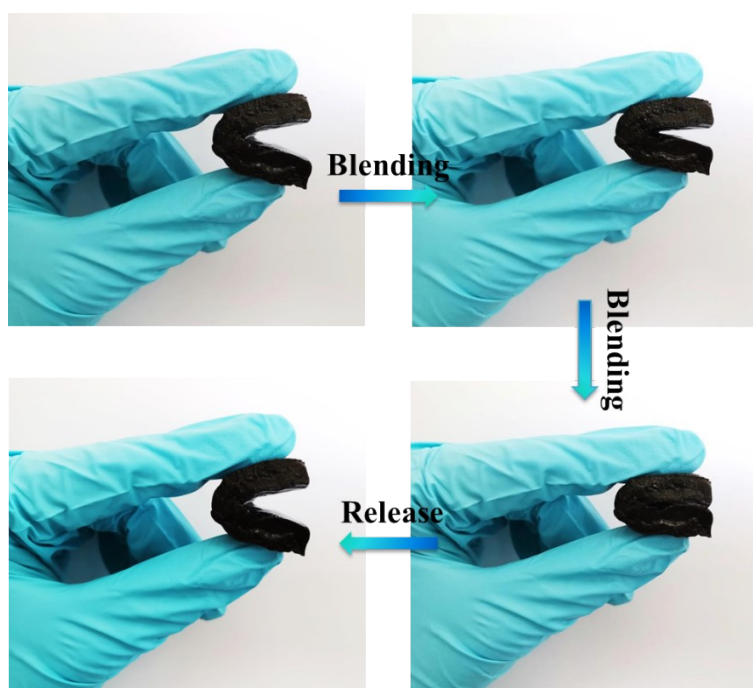


Fig. S41 Photographs of CPP bending and release.

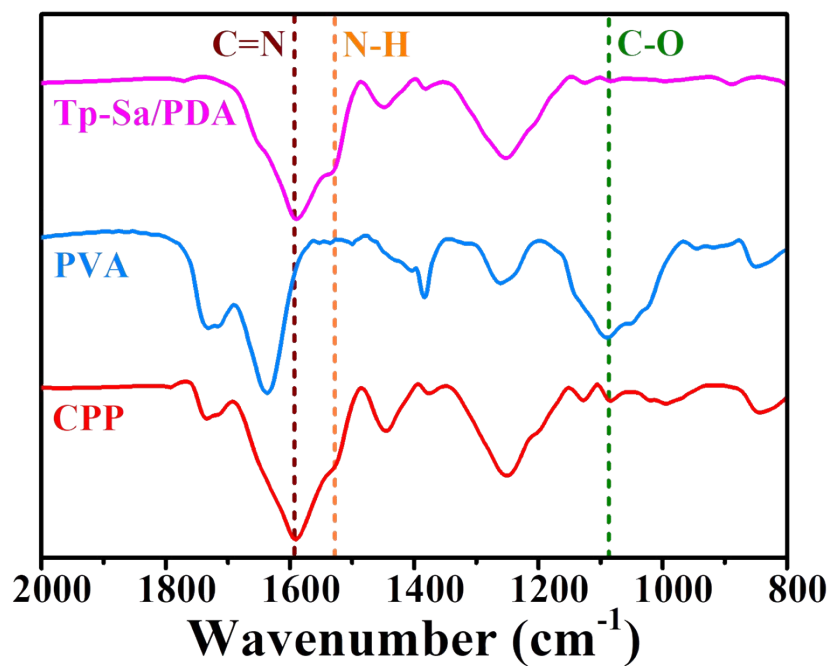


Fig. S42 FT-IR spectra of Tp-Sa/PDA, PVA and CPP.

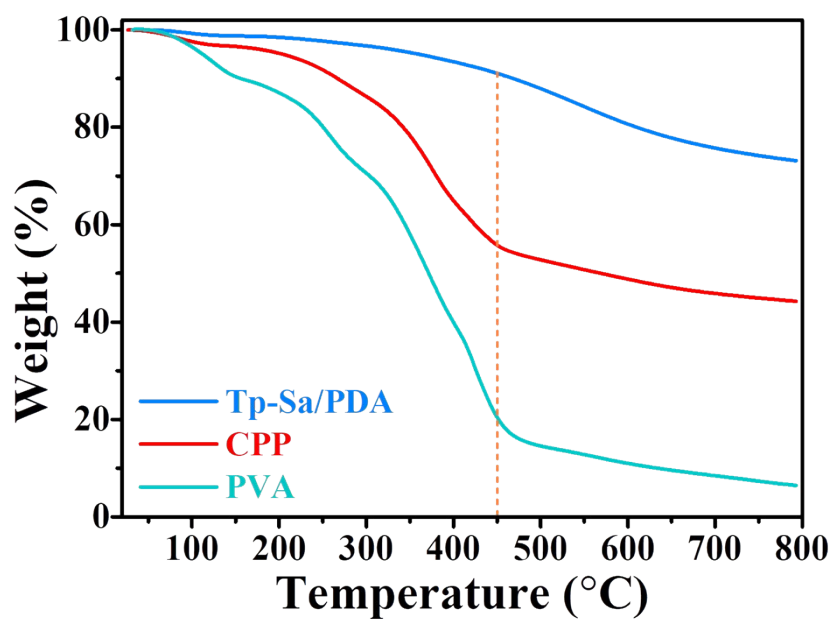


Fig. S43 TGA curves of Tp-Sa/PDA, CPP and PVA.

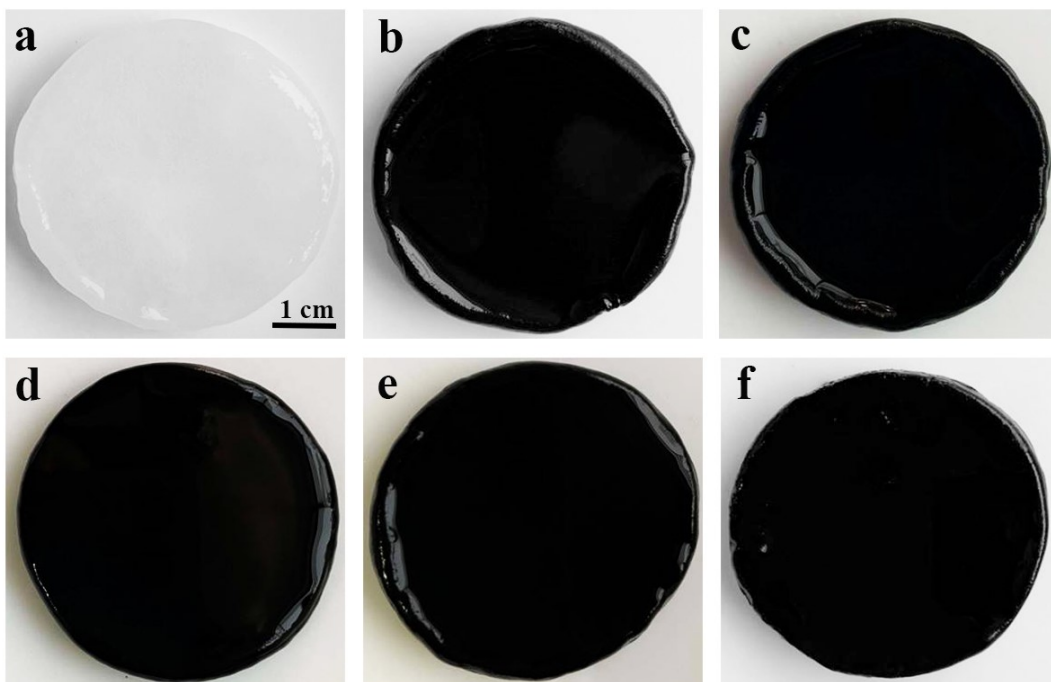


Fig. S44 Photographs of PVA (a), 0.1 CPP (b), 0.2 CPP (c), 0.3 CPP (d), 0.4 CPP (e), and 0.5 CPP (f).

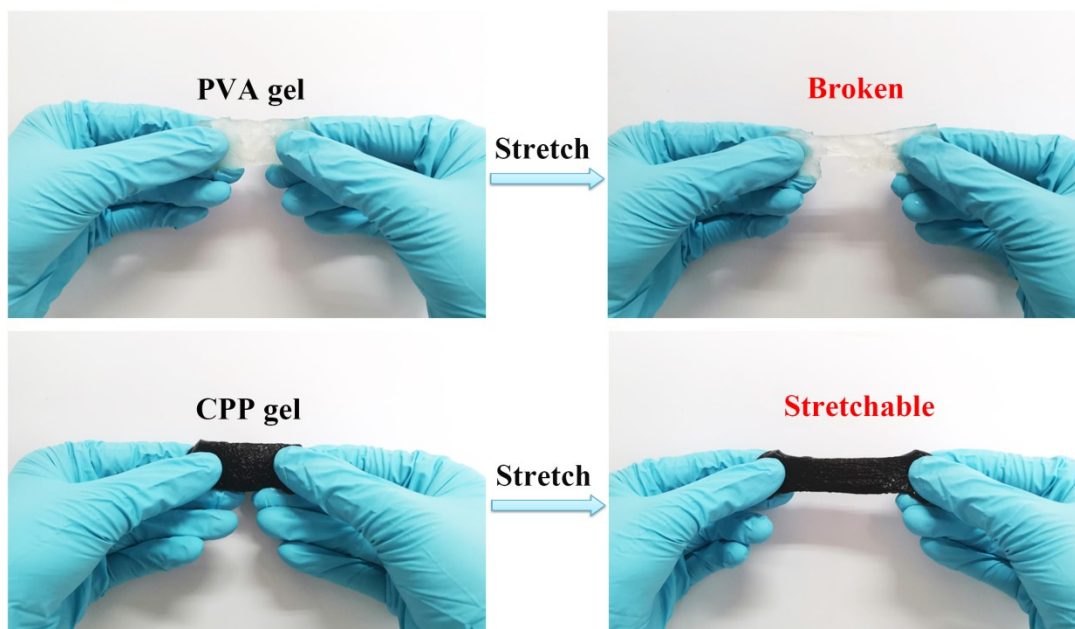


Fig. S45 Stretchable tests of PVA hydrogel and CPP hydrogel.

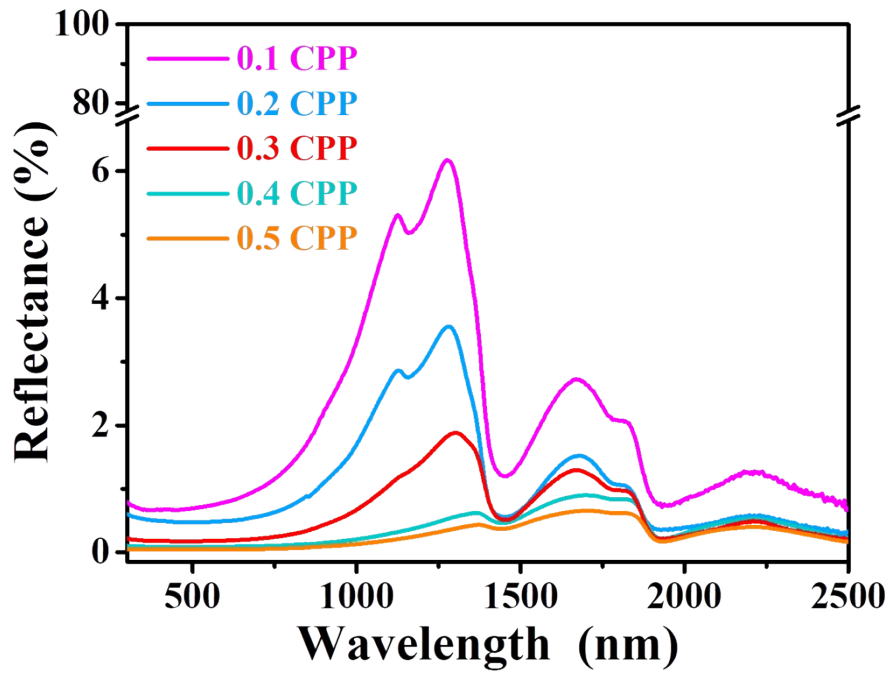


Fig. S46 Reflectance spectra of the CPPs.

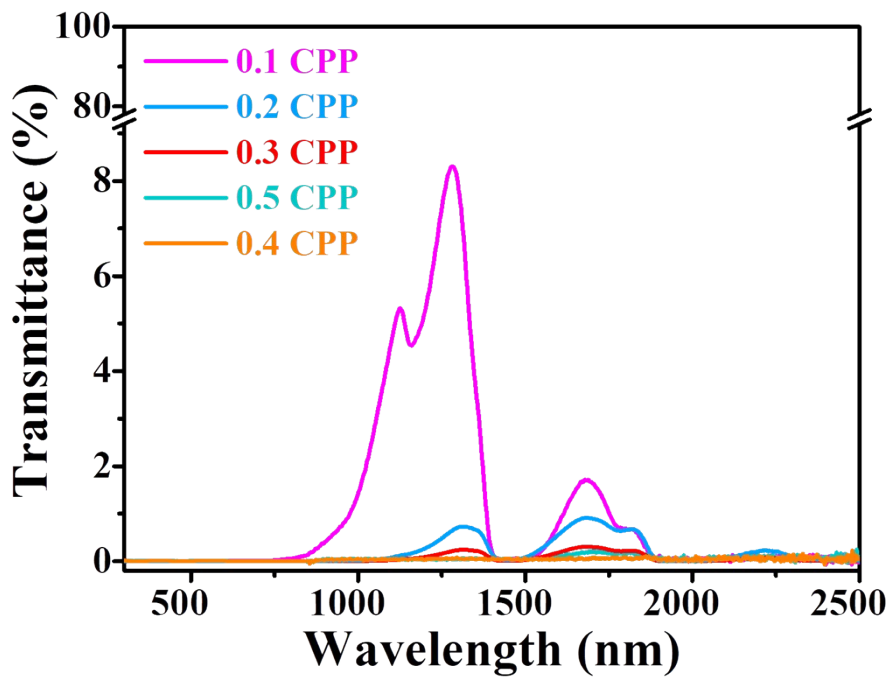


Fig. S47 Transmittance spectra of the CPPs.

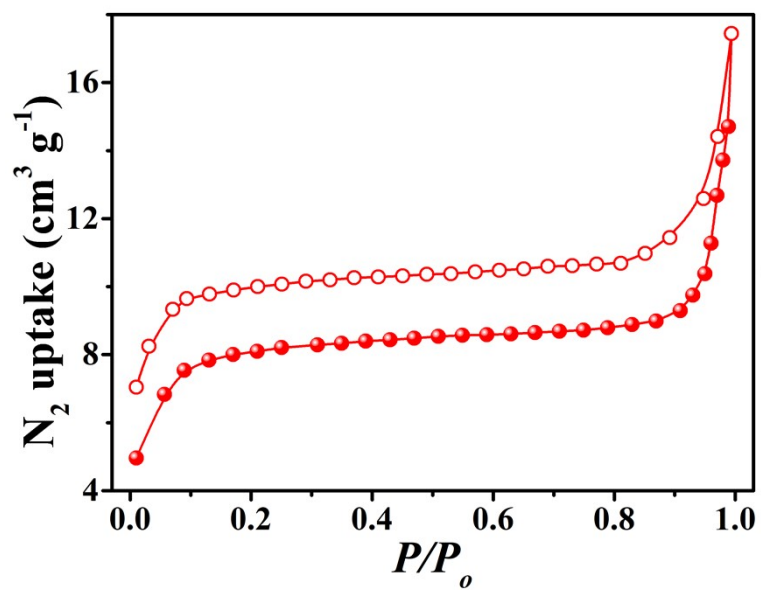


Fig. S48 N₂ adsorption–desorption isotherms of CPP.

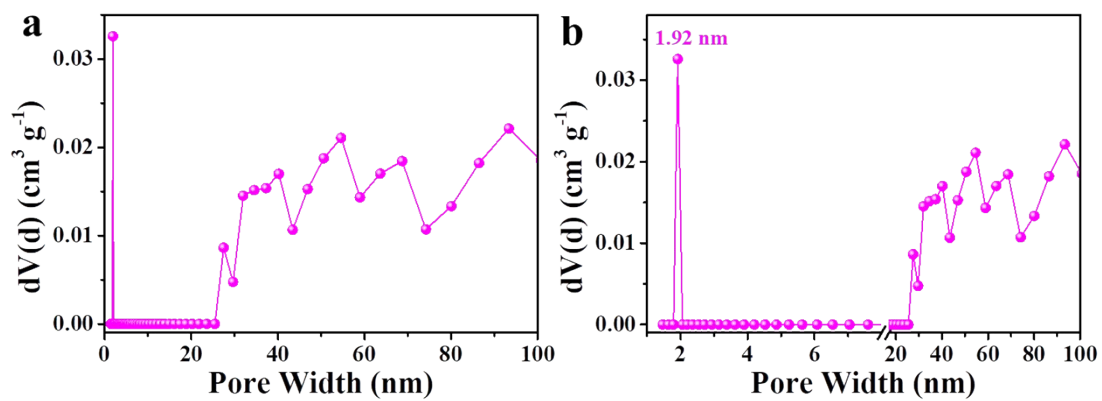


Fig. S49 (a, b) Pore-size distribution profiles of CPP.

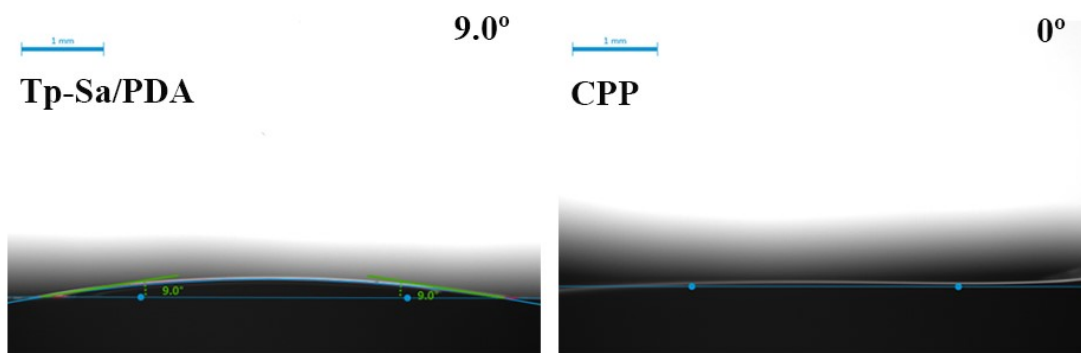


Fig. S50 Static water contact angles of Tp-Sa/PDA and CPP.

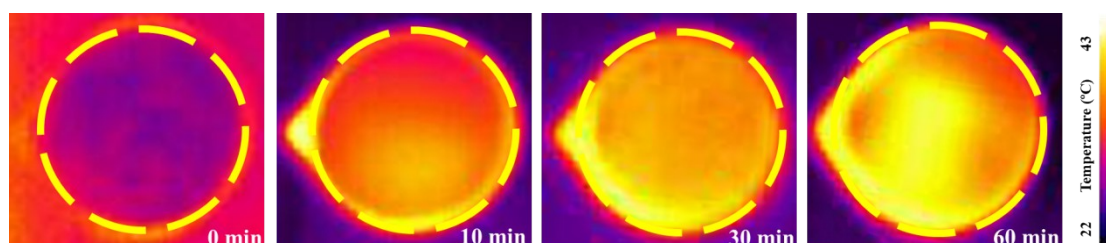


Fig. S51 The corresponding infrared images showed the temperature distribution, and the visible light irradiation time was 0, 10, 30 and 60 min, respectively. The optical intensity was set to be 1 kW m^{-2} .

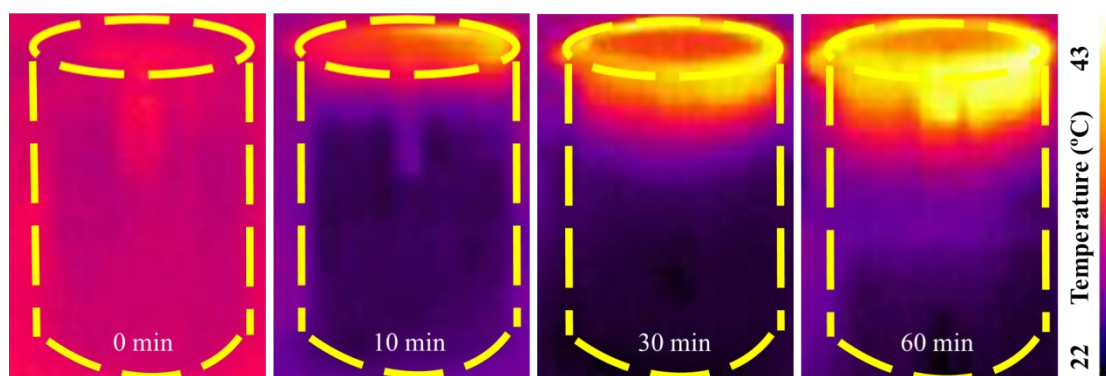


Fig. S52 The corresponding infrared images showed the temperature distribution, and the visible light irradiation time was 0, 10, 30 and 60 min, respectively. The optical intensity was set to be 1 kW m^{-2} .

Table S3 Evaporation rate (m) and efficiency (η) of recently reported solar steam generation materials under one sun.

Evaporator	m (kg m⁻² h⁻¹)	η (%)	Ref.
CPP	1.50	91.5%	This Work
SCF	1.96	94.5%	2
c-CNT	1.41	95.8%	3
PNPG	1.72	93.5%	4
M-Ag-CNT	1.70	95.0%	5
AFC-I	1.46	91.7%	6
MWCNTs-COOH/CF	1.18	86.0%	7
CuS/BC	1.44	83.5%	8
CL-500 sponge	1.36	83.7%	9
MoS₂ aerogels	1.27	88.0%	10
PPy-wood	1.01	72.5%	11

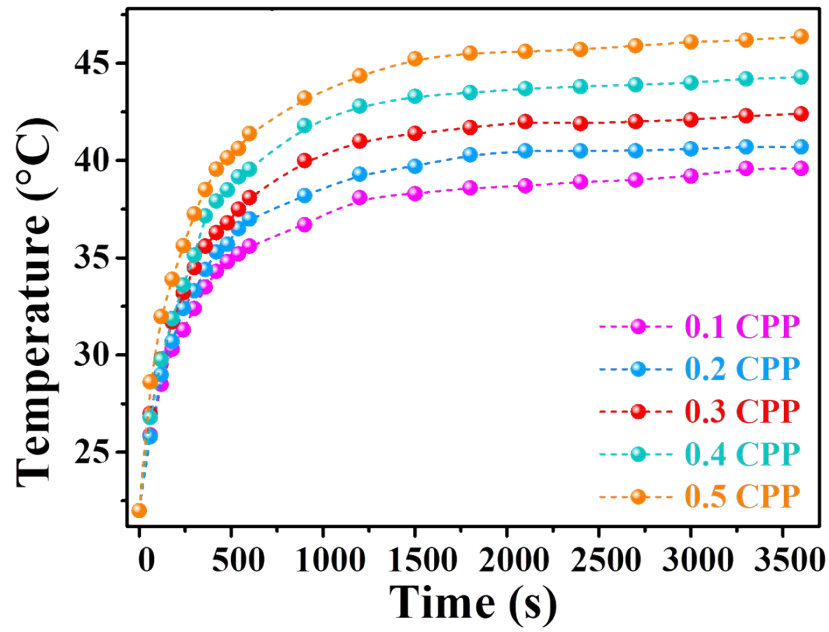


Fig. S53 The surface temperature of CPP at different optical densities of 1-5 kW m⁻².

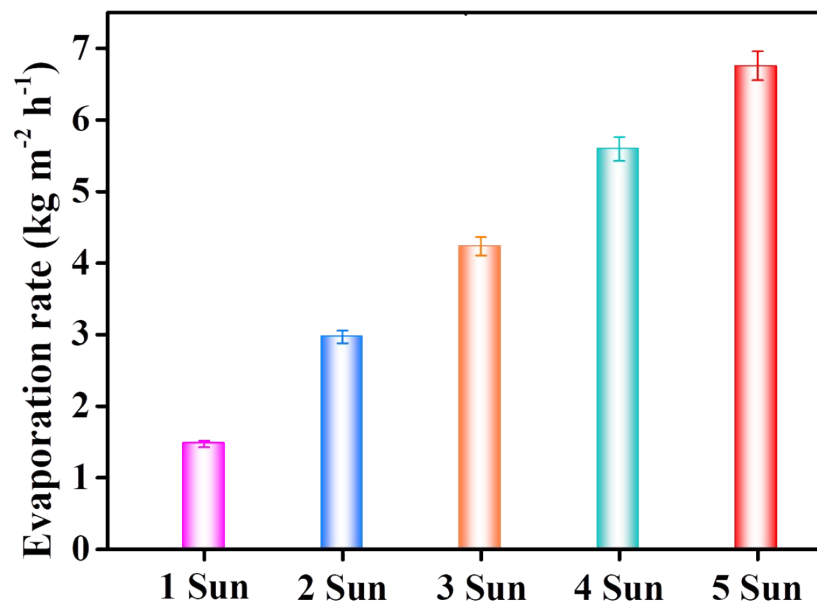


Fig. S54 The water evaporation rate of CPP at different optical densities of 1-5 kW m⁻².

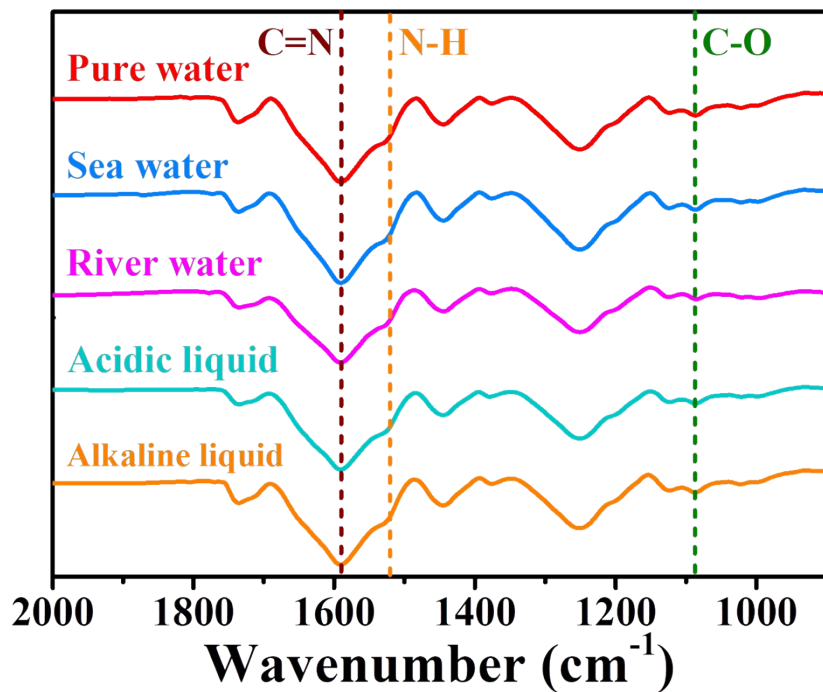


Fig. S55 FT-IR spectra of CPP after evaporating in different types of water.

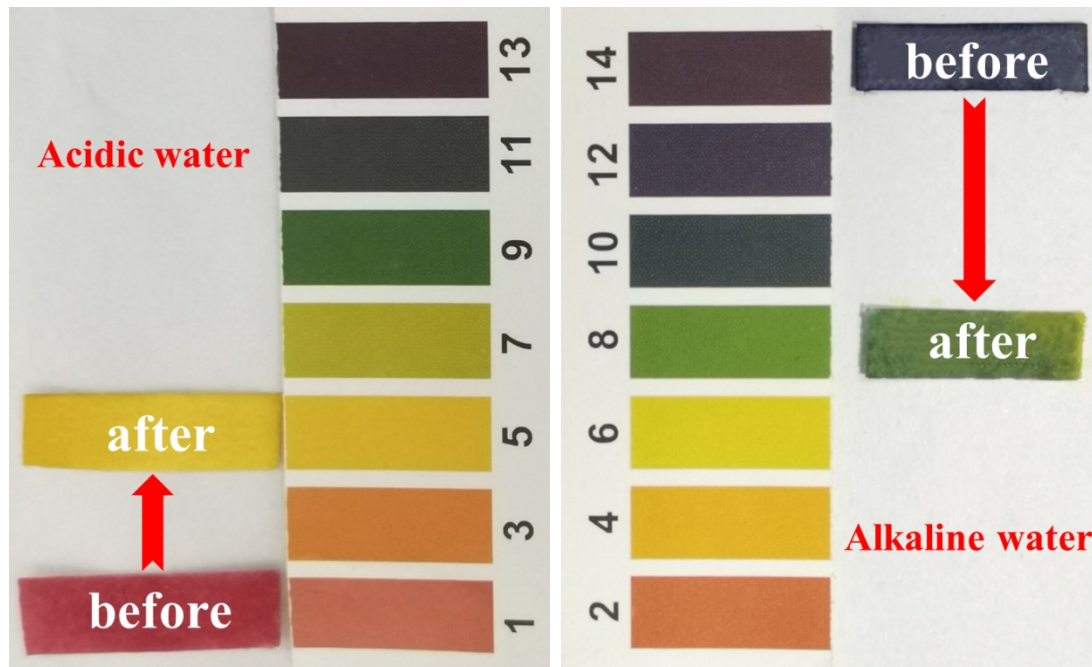


Fig. S56 Photographs of pH papers tested in acidic water or alkaline water before and after evaporation.

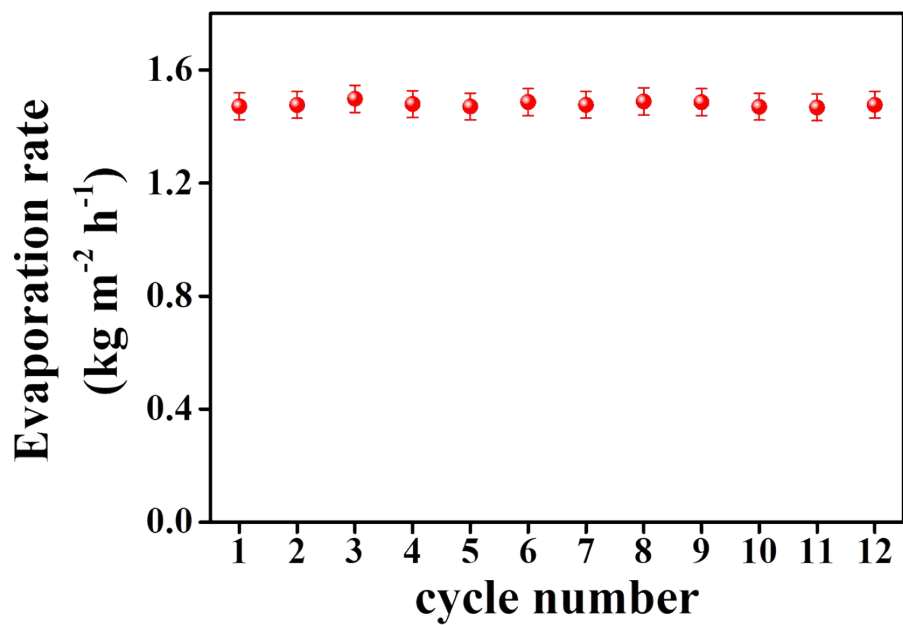


Fig. S57 Cycling performance of solar evaporation rate of CPP in natural seawater.



Fig. S58 The NaCl salt was added on the surface of CPP that was floating on the salty water before exposure to solar irradiation.

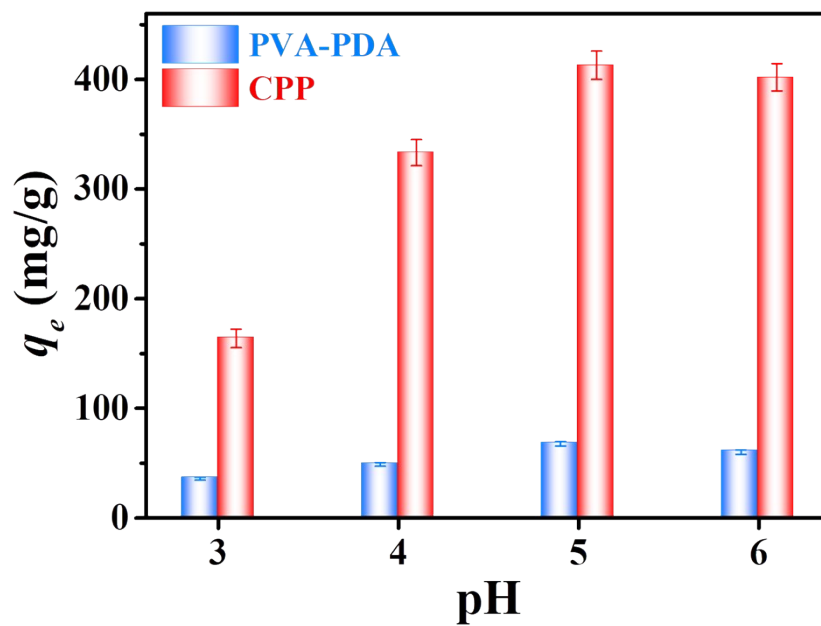


Fig. S59 Optimal pH for uranium extraction of 0.3 CPP and PVA-PDA hydrogel in uranium spiked filtered natural seawater.

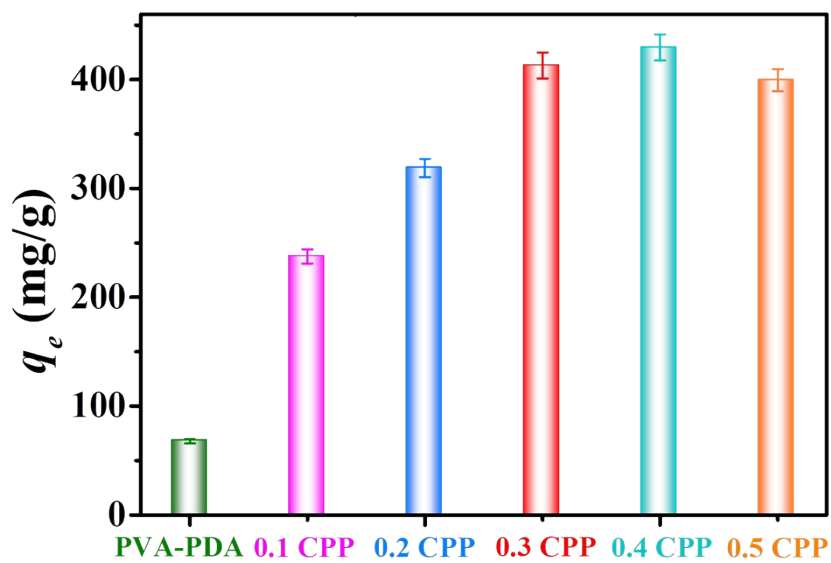


Fig. S60 The uranium adsorption capacity of different CPP hydrogels in uranium spiked filtered natural seawater at pH 5.0.

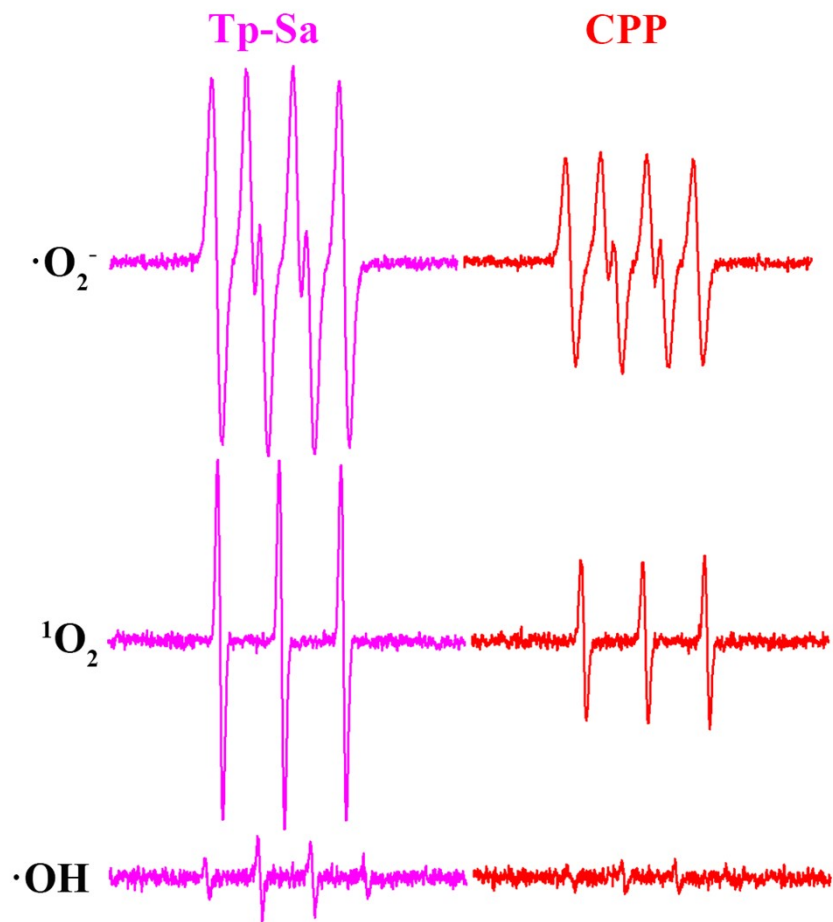


Fig. S61 Production of ROS under visible light irradiation.

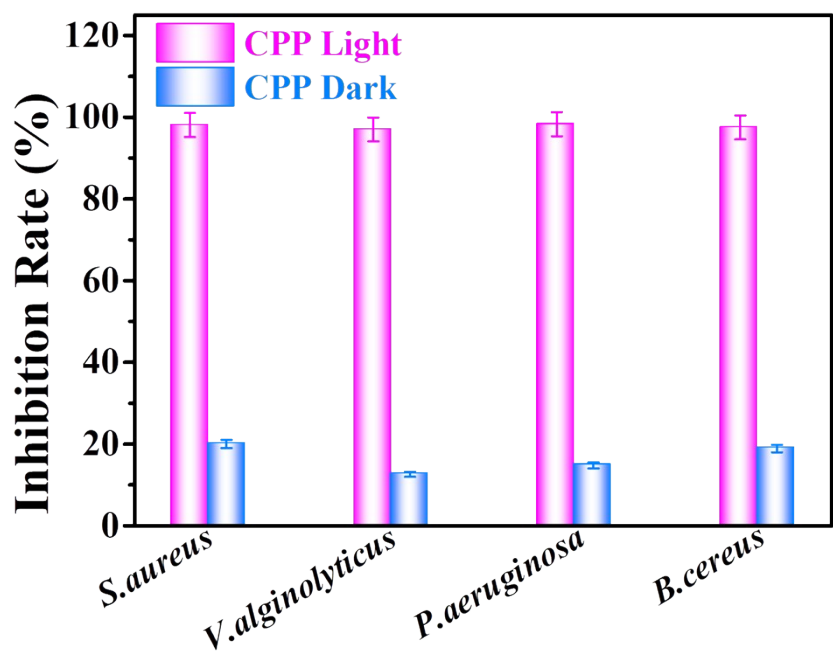


Fig. S62 Anti-bacterial spectrum.

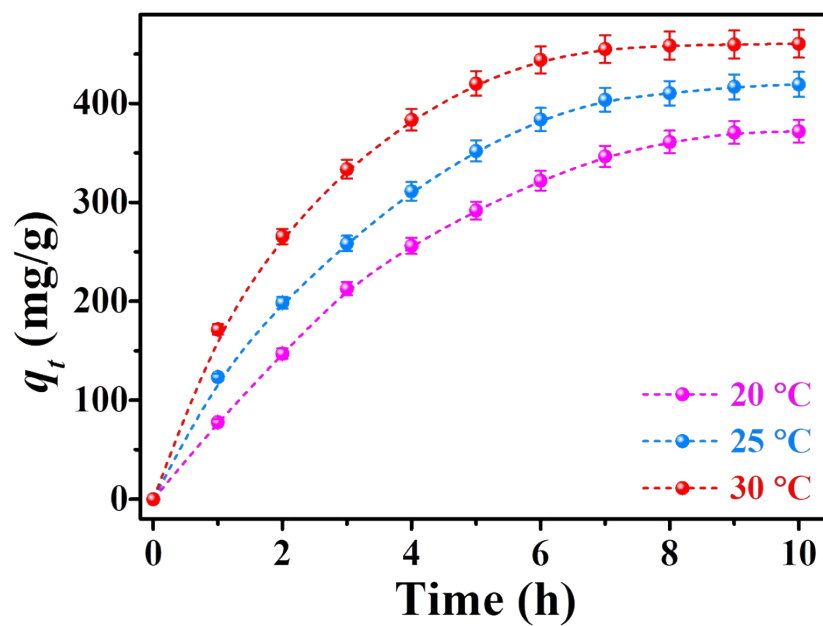


Fig. S63 The influence of temperature on the uranium adsorption performance of CPP. The uranium adsorption experiments were performed in uranium spiked filtered natural seawater under dark conditions.

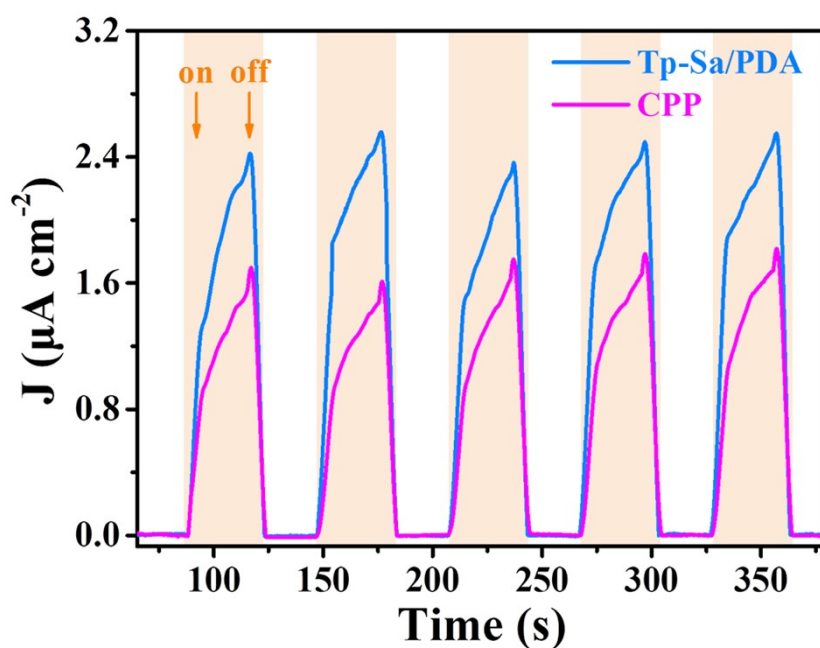


Fig. S64 Transient photocurrent response of Tp-Sa/PDA and CPP.

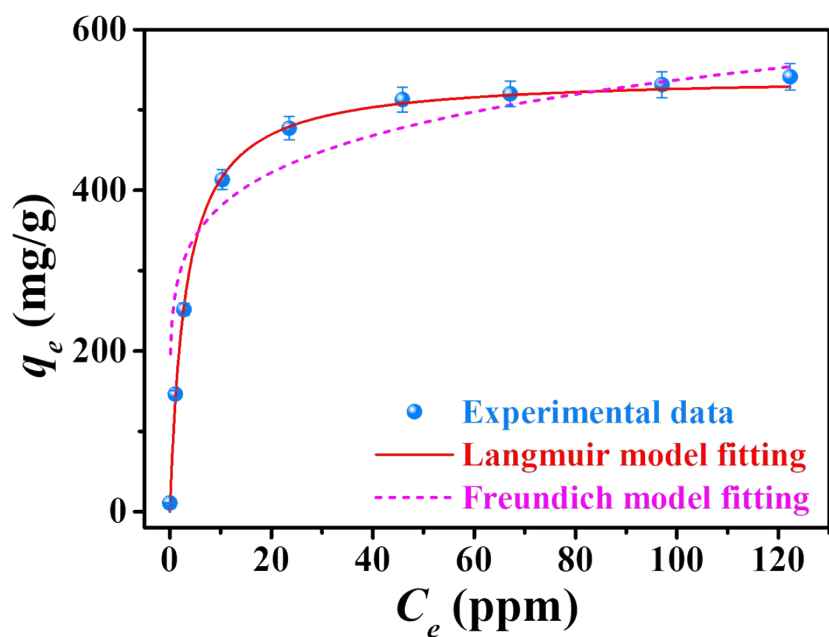


Fig. S65 The adsorption performances of CPP after treatment in different uranium spiked filtered natural seawater under visible light irradiation.

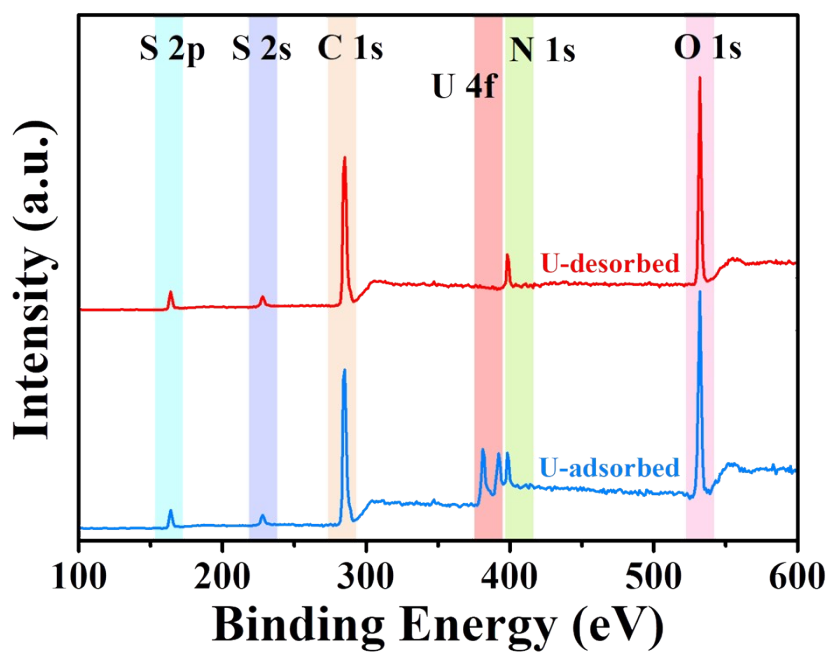


Fig. S66 XPS survey spectra of CPP measured before and after desorption of uranium.

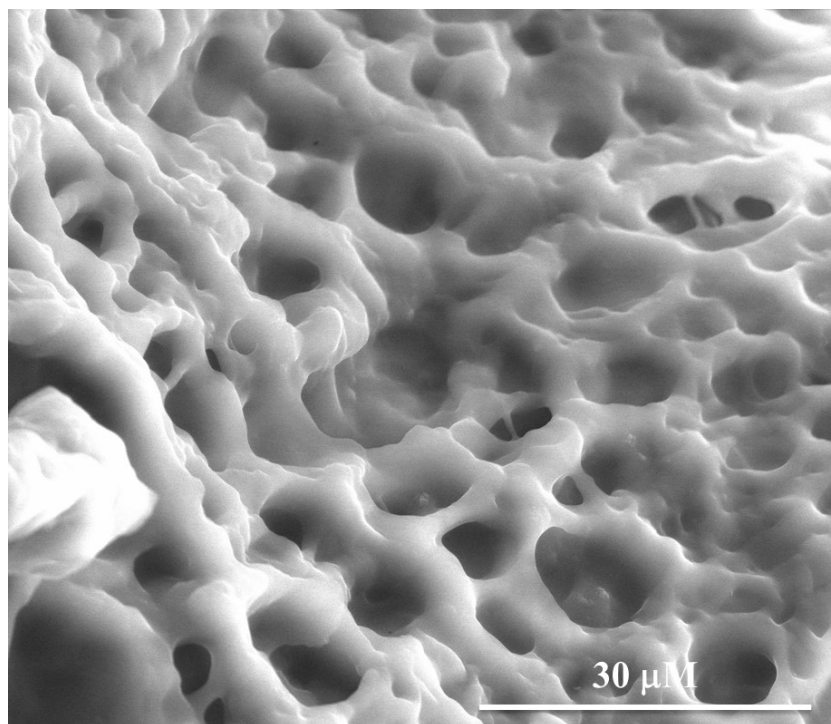


Fig. S67 The SEM image of CPP after desorption of uranium by the elution solution of ascorbic acid (0.5 M) and HNO₃ (0.1 M).

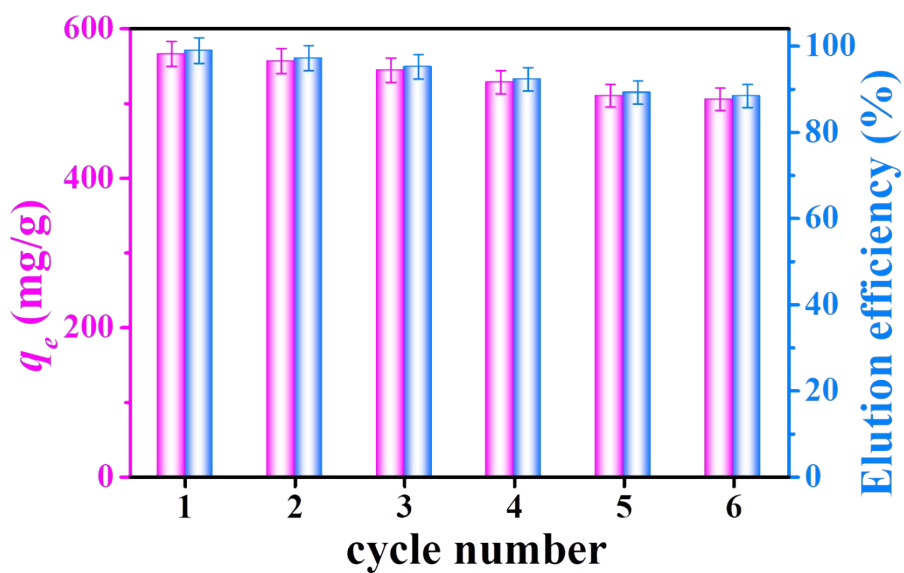


Fig. S68 The uranium adsorption capacity and elution efficiency of CPP.



Fig. S69 The prototype for concurrent seawater desalination and uranium extraction under natural sunlight. The CPP floats on seawater in a container that is located in a holder with meshes. The vapor is condensed via the transparent condenser and flows to the bottom of the prototype, where the purified water is stored. Brine is supplied and fresh water collected at optimum rates through the inlet pipe and outlet pipe, respectively. A sustained water purification system and uranium extraction was achieved under natural sunlight.

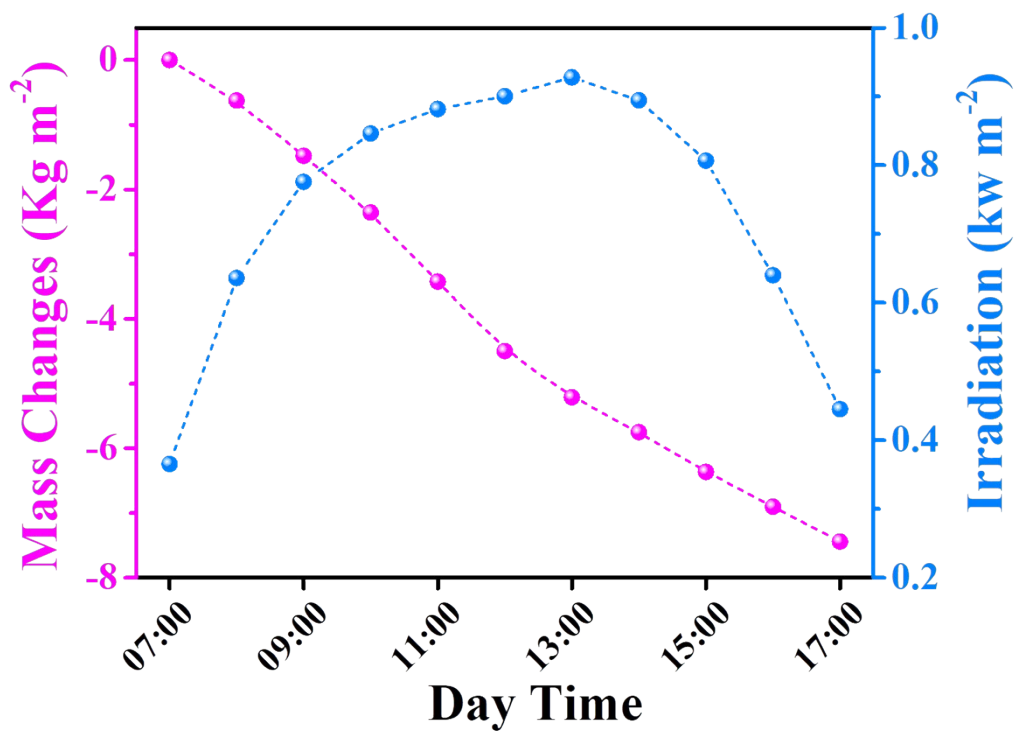


Fig. S70 Water mass change of BHMS3 evaporator and solar intensity record as a function of time within 10 h.

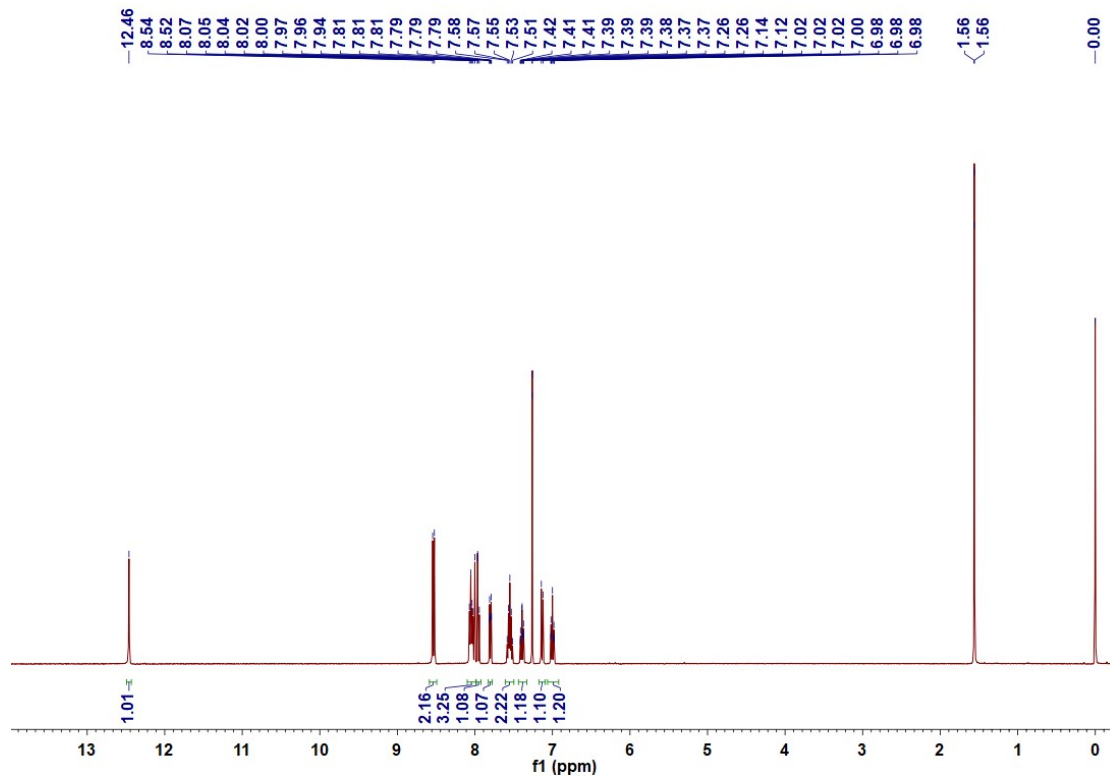


Fig. S71 ¹H NMR spectra of Model Compound M1 in CDCl₃.

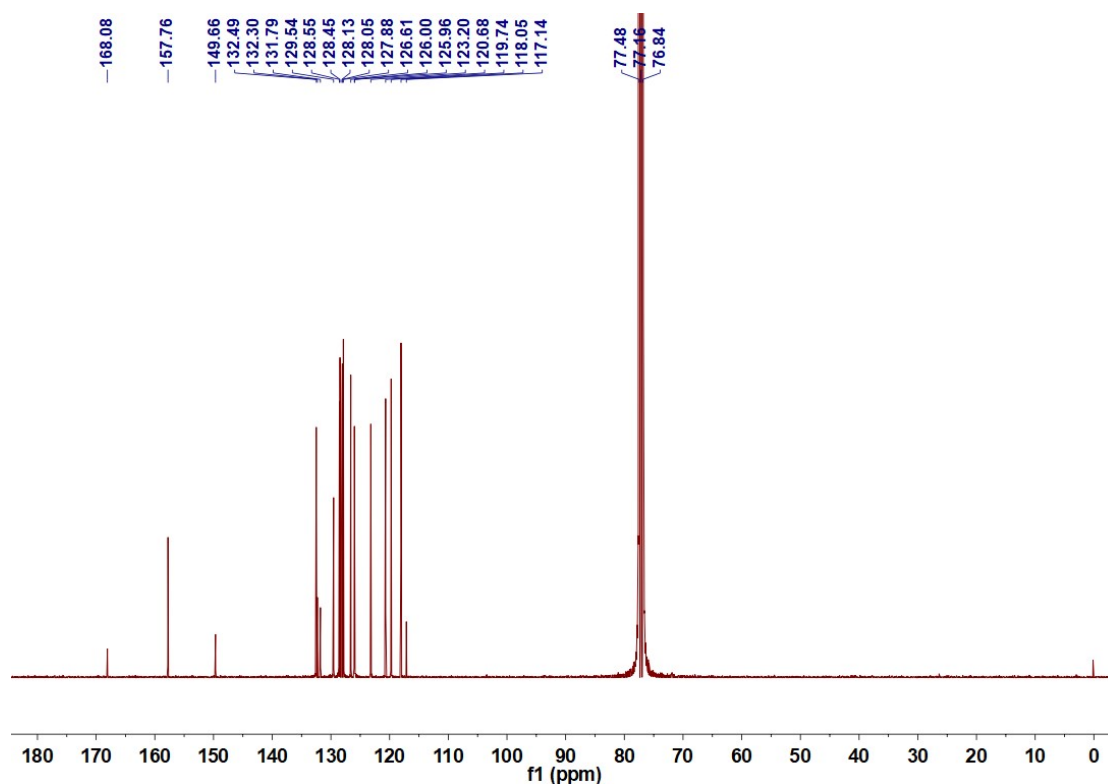


Fig. S72 ^{13}C NMR spectra of Model Compound M1 in CDCl_3 .

References

- 1 W.-R. Cui, F.-F. Li, R.-H. Xu, C.-R. Zhang, X.-R. Chen, R.-H. Yan, R.-P. Liang, J.-D. Qiu, *Angew. Chem. Int. Ed.*, 2020, **59**, 17684-17690.
- 2 W. Huang, P. Su, Y. Cao, C. Li, D. Chen, X. Tian, Y. Su, B. Qiao, J. Tu, X. Wang. *Nano Energy*, 2020, **69**, 104465.
- 3 K. Li, M. Gao, Z. Li, H. Yang, L. Jing, X. Tian, Y. Li, S. Li, H. Li, Q. Wang, J. S. Ho, G. W. Ho, P.-Y. Chen, *Nano Energy*, 2020, **74**, 104875.
- 4 Z. Lin, T. Wu, J. Shi, B. Zhou, C. Zhu, Y. Wang, R. Liang, M. Mizuno, *ACS Sustain. Chem. Eng.*, 2021, **9**, 448-457.
- 5 X. Zhao, C. Liu. *Solar Energy*, 2020, **195**, 304-309.
- 6 X. Wang, Q. Gan, R. Chen, H. Peng, T. Zhang, M. Ye, *ACS Sustain. Chem. Eng.*, 2020, **8**, 7753-7761.
- 7 Q. Qi, Y. Wang, W. Wang, X. Ding, D. Yu. *Sci. Total Environ.*, 2020, **698**, 134136.
- 8 D. Zhang, M. Zhang, S. Chen, Q. Liang, N. Sheng, Z. Han, Y. Cai, H. Wang. *Desalination*, 2021, **500**, 114899.
- 9 R. Wen, Y. Li, M. Zhang, X. Guo, X. Li, X. Li, J. Han, S. Hu, W. Tan, L. Ma, S. Li, *J. Hazard. Mater.*, 2018, **358**, 273-285.
- 10 Q. Wang, Q. Guo, F. Jia, Y. Li, S. Song, *ACS Appl. Mater. Interfaces*, 2020, **12**, 32673-32680.
- 11 Z. Wang, Y. Yan, X. Shen, C. Jin, Q. Sun, H. Li. *J. Mater. Chem. A*, 2019, **7**, 20706-20712.